

MODELING AND SIMULATIONS OF DIRECT STEAM GENERATION IN
CONCENTRATING SOLAR POWER PLANTS USING PARABOLIC TROUGH
COLLECTORS

A THESIS SUBMITTED TO
THE GRADUATE SCHOOL OF NATURAL AND APPLIED SCIENCES
OF
MIDDLE EAST TECHNICAL UNIVERSITY

BY

CAN UÇKUN

IN PARTIAL FULFILLMENT OF THE REQUIREMENTS
FOR
THE DEGREE OF MASTER OF SCIENCE
IN
MECHANICAL ENGINEERING

MARCH 2013

Approval of the thesis:

**MODELING AND SIMULATIONS OF DIRECT STEAM GENERATION IN SOLAR
POWER PLANTS USING PARABOLIC TROUGH COLLECTORS**

Submitted by **CAN UÇKUN** in partial fulfillment of the requirements for the degree of
**Master of Science in Mechanical Engineering Department, Middle East Technical
University** by,

Prof. Dr. Canan Özgen
Dean, Graduate School of **Natural and Applied Sciences**

Prof. Dr. Suha Oral
Head of Department, **Mechanical Engineering**

Assoc. Prof. Dr. Derek K. Baker
Supervisor, **Mechanical Engineering Dept., METU**

Examining Committee Members:

Prof. Dr. Raşit Turan
Physics Dept., METU

Assoc. Prof. Dr. Derek K. Baker
Mechanical Engineering Dept., METU

Assist. Prof. Dr. Tuba Okutucu
Mechanical Engineering Dept., METU

Assist. Prof. Dr. Metin Yavuz
Mechanical Engineering Dept., METU

Instructor Dr. Özgür Bayer
Mechanical Engineering Dept., METU

Date:

18 – 03 – 2013

I hereby declare that all information in this document has been obtained and presented in accordance with academic rules and ethical conduct. I also declare that, as required by these rules and conduct, I have fully cited and referenced all material and results that are not original to this work.

Name, Last name : Can UÇKUN

Signature :

ABSTRACT

MODELING AND SIMULATIONS OF DIRECT STEAM GENERATION IN CONCENTRATING SOLAR POWER PLANTS USING PARABOLIC TROUGH COLLECTORS

Uçkun, Can

M.Sc., Department of Mechanical Engineering

Supervisor: Assoc. Prof. Dr. Derek K. Baker

March 2013, 65 pages

In this thesis, a mathematical model of direct steam generation using parabolic trough collectors is developed. The model's predictions are compared with previously published data and good agreement is found. A parametric study for direct steam generation in parabolic trough collectors is presented for different inlet temperature and pressures, and solar resources, and the differences between the conditions are analyzed. The direct steam generation mathematical model is integrated into a TRNSYS model of a complete solar thermal power plant. The predictions for this model of a complete solar thermal power plant are compared with previously published and acceptable results are found. The implications for this work are discussed and future research directions identified.

Keywords: Solar Energy, Direct Steam Generation, Concentrating Solar Thermal Energy, Parabolic Trough Collector.

ÖZ

YOĞUNLAŞTIRILMIŞ GÜNEŞ ENERJİSİ SANTRALLRİNDE PARABOLİK OLUKLU KOLEKTÖRLER KULLANILARAK DİREK BUHAR ÜRETİMİNİN MODELLENMESİ VE SİMÜLASYONU

Uçkun, Can
Yüksek Lisans, Makina Mühendisliği Bölümü
Tez Yöneticisi: Doç. Dr. Derek K. Baker

Mart 2013, 65 sayfa

Bu çalışmada, parabolik oluklu kolektörler kullanılarak direk buhar üretiminin matematiksel modeli sunulmaktadır. Oluşturulan matematiksel model daha önce yayınlanmış çalışma ile karşılaştırılmıştır ve sonuçlar iyi uyumluluk göstermiştir. Oluşturulan model, farklı basınçlar, giriş sıcaklıkları ve farklı güneş enerjisi kaynakları kullanılarak parametrik çalışma yapılmış ve durumlar arasındaki farklar analiz edilmiştir. Direk buhar üretimi matematiksel modeli, TRNSYS programı kullanılarak termal güneş enerjisi santrali ve buhar üretimi modellenmesi için kullanılmış ve sonuçlar daha önce yayınlanmış benzer çalışma ile karşılaştırılmıştır. Sonuçlar tartışılmış ve gelecekteki araştırmalar için izlenilebilecek yollar belirlenmiştir.

Anahtar kelimeler: Güneş Enerjisi, Direk Buhar Üretimi, Yoğunlaştırılmış Güneş Enerjisi, Parabolik Oluklu Kolektör,

Dedicated to My Family

ACKNOWLEDGEMENTS

First, I express my sincere appreciation to my thesis supervisor Assoc. Prof. Dr. Derek BAKER for his guidance, patience, encouragement and advices for the entire progress of this thesis study, keep me going.

I would like to thank my family for having supported me throughout my life with patience and love.

Additionally, I would like to thank Tuğrul MARAL for his friendship, encouragement and guidance.

I want to thank my friends Mesru ALTINÖZ, Koray TAŞTANKAYA, Tufan AKBA and Erdem Emre PINAR for their friendship and cooperation throughout the master program.

I am also appreciated to all of my colleagues in CERES (Clean Energy Research Education and Service) group for sharing ideas.

Finally, I would like to thank GÜNAM (Center for Solar Energy Research and Applications) for providing TRNSYS software.

TABLE OF CONTENTS

ABSTRACT.....	v
ÖZ	vi
ACKNOWLEDGEMENTS	viii
TABLE OF CONTENTS.....	ix
LIST OF TABLES	x
LIST OF FIGURES	xi
LIST OF SYMBOLS	xiii
CHAPTERS	
1.INTRODUCTION.....	1
1.1. Motivation.....	1
1.2. Literature Review	6
1.2.1. Principles of CSP Technologies	6
1.2.2. Solar Power Tower.....	8
1.2.3. Parabolic Dish.....	10
1.2.4. Fresnel.....	11
1.2.5. Parabolic Trough.....	11
1.2.6. Direct Steam Generation in Concentrating Solar Thermal Power Plants.....	13
1.2.7. PTC Solar Thermal Power Plant Models	16
1.2.8. Thesis Objective.....	16
2.DSG MODELING	17
2.1 Collector Model.....	17
2.1.1 Solar Resources.....	17
2.1.2 Flow In a DSG Collector.....	22
2.1.3 Heat Losses	24
2.1.4 Heat Transfer to the Working Fluid	26
2.1.5 Pressure Drop	29
2.1.6 Computer Code.....	32
2.1.7 Benchmarking.....	36
3.DSG SIMULATIONS	37
3.1 Parametric Studies	37
4.CSP MODEL AND SIMULATIONS	47
4.1 Simulation of a Solar Array	47
4.2 Simulation of a CSP Power Plant.....	50
5.CONCLUSION AND FUTURE WORK	61
REFERENCES	62

LIST OF TABLES

TABLES

Table 1.1 Properties of CSP Technologies available [7].....	8
Table 2.1 Thermal Conductivity of AISI 304 Steel	28
Table 2.2 Design Point Parameters [21].....	32
Table 2.3 Parameters of ET-100 Parabolic Trough Collectors [21].....	32
Table 2.4 Inlet Conditions for Design [21].....	33
Table 2.5 Benchmarking Outlet of Preheat-Boiling Section.....	36
Table 2.6 Benchmarking Outlet of First Superheating Section.....	36
Table 2.7 Benchmarking Outlet of Second Superheating Section.....	36
Table 3.1 Results for Inlet pressure of 60 bars	38
Table 3.2 Results for Inlet pressure of 80 bars	39
Table 3.3 Results for Inlet pressure of 100 bars	40
Table 3.4 Results for Inlet pressure of 120 bars	41
Table 3.5 Results for DNI=400 W/m ²	42
Table 3.6 Results for DNI=600 W/m ²	43
Table 3.7 Results for DNI=800 W/m ²	44
Table 3.8 Results for DNI=1000 W/m ²	45
Table 4.1 Geographical Information of Almeria Airport	49
Table 4.2 Input to Type 155 from Weather Data	49
Table 4.3 Component Connections of the Solar Collector Array Model.....	49
Table 4.4 Component Connections of Power Pant Model	53
Table 4.5 Data Used for System Efficiency Calculations.....	59

LIST OF FIGURES

FIGURES

Figure 1.1 CO ₂ Emissions by Year [2]	3
Figure 1.2 First Solar Thermal Facility in Egypt [4].....	4
Figure 1.3 Main Sources of Carbon Emissions in 2008 [2]	5
Figure 1.4 Diffuse and Beam Radiation	6
Figure 1.5 Receiver and Aperture Area of a PTC	7
Figure 1.6 Tracking in a CSP Collector.....	8
Figure 1.7 Solar Power Tower [8].....	9
Figure 1.8 Parabolic Dish [13].....	10
Figure 1.9 Fresnel Collectors [15].....	11
Figure 1.10 Parabolic Trough Collector [16].....	12
Figure 1.11 DISS Facility [19].....	14
Figure 1.12 Schematic Representation of Solar Array in INDITEP Project [21]	15
Figure 2.1 Solar Angles.....	18
Figure 2.2 Declination Angle [28]	18
Figure 2.3 Angle of Incidence and Zenith Angle.....	19
Figure 2.4 N-S and E-W Axis Tracking	20
Figure 2.5 Comparisons of N-S and E-W Axis Tracking by Month	22
Figure 2.6 Two Phase Flow Regimes [33]	23
Figure 2.7 Two Phase Flow in a Horizontal Tube [22].....	24
Figure 2.8 Thermal and Optical Losses on Absorber Tube [22].....	25
Figure 2.9 Relative Roughness versus Pipe Diameter For Different Pipe Materials [31]	30
Figure 2.10 Connection Between Sub-modules	33
Figure 2.11 Flow Chart of the Matlab Code	35
Figure 3.1 Thermal Power Produced and Efficiency for Variable Inlet Temperatures for 60 Bars Inlet Pressure.....	38
Figure 3.2 Thermal Power Produced and Efficiency for Variable Inlet Temperatures for 80 Bars Inlet Pressure	39
Figure 3.3 Thermal Power Produced and Efficiency for Variable Inlet Temperatures for 100 Bars Inlet Pressure.....	40
Figure 3.4 Thermal Power Produced and Efficiency for Variable Inlet Temperatures for 120 Bars Inlet Pressure	41
Figure 3.5 Thermal Power Produced and Efficiency for Variable Inlet Temperatures for	42
Figure 3.6 Thermal Power Produced and Efficiency for Variable Inlet Temperatures for	43
Figure 3.7 Thermal Power Produced and Efficiency for Variable Inlet Temperatures for	44
Figure 3.8 Thermal Power Produced and Efficiency for Variable Inlet Temperatures for	45
Figure 4.1 Schematic Representation of DSG Solar Array Model	47
Figure 4.2 TRNSYS Model of Solar Array	48
Figure 4.3 Simulation Results for 26 June	50
Figure 4.4 Schematic of CSP Solar Power Plant Model.....	51
Figure 4.5 Sample TRNSYS Model Used in Both Cases of Simulation.....	52

Figure 4.6 DNI for TMY2 Data and Reference Simulation for June 12.....	54
Figure 4.7 Simulation Result of June 12 for Almeria Airport TMY Data (case 1)	54
Figure 4.8 Published Simulation Results of June 12 for PSA Site [21]	55
Figure 4.9 Simulation Result of June 12 for Almeria Airport TMY Data (case 2)	56
Figure 4.10 DNI for TMY2 Data and Reference Simulation for Clear Winter Day (February 3- January 29)	57
Figure 4.11 Simulation Result of February 3 for Almeria Airport TMY Data (case 1)	57
Figure 4.12 Published Simulation Results of January 29 for PSA Site [21]	58
Figure 4.13 Simulation Result of February 3 for Almeria Airport TMY Data (case 2)	59

LIST OF SYMBOLS

h	enthalpy (kJ kg^{-1})
L_{st}	standard meridian for the local time zone (deg)
L_{loc}	the longitude of the location (deg)
\dot{m}	mass flowrate (kg s^{-1})
n	day number of the year
P	pressure (bar)
Q	heat transfer (kJ)
Θ	angle of incidence
θ_z	zenith angle
T	temperature ($^{\circ}\text{C}$)
Fr	Froude number
X_{tt}	Martinelli parameter
Re	Reynolds number
G_{sc}	Solar constant (Wm^{-2})
U	overall heat transfer coefficient ($\text{Wm}^{-2}\text{K}^{-1}$)
K	thermal conductivity ($\text{Wm}^{-1}\text{K}^{-1}$)
We	Weber number
h	convection heat transfer coefficient ($\text{Wm}^{-2}\text{K}^{-1}$)
r	radius (m)
x	steam quality

Greek Symbols

ω	hour angle
ϕ	latitude
δ	declination angle (deg)
μ	efficiency
γ	surface azimuth angle (deg)
ϵ	emissivity
ρ	density (kg m^{-3})

Subscripts

in	inlet
max	maximum
min	minimum
e	exit
l	liquid
g	gas
1ph	one phase
2ph	two phase
ab	absorber
dp	dew point
amb	ambient
m	mean
ave	average
inj	injected
sh	superheated
fw	feedwater

Abbreviations

CSP	concentrating solar power
DNI	direct normal irradiance
DSG	direct steam generation
FWH	feedwater heater
HTF	heat transfer fluid
HP	high pressure
LP	low pressure
PTC	parabolic trough collector
SEGS	solar energy generating systems
TMY	typical metrological year
ISCC	integrated solar combined cycle
DISS	direct solar steam

CHAPTER I

INTRODUCTION

1.1. Motivation

Energy has been one of the most important issues since people started to build civilizations. People cannot sustain all their needs with their own energy. So people are always searching to find easy ways to meet their energy demands. People need energy supplied from another source to make their lives easier. It can either be as simple as fire, which is supplied by wood to cook a meal or avoid cold weather, or be a coal fired power plant to produce electricity to meet the same demands. The common feature for these two cases is the need for an energy source to meet the same demands which people cannot meet by themselves. The first example represents early cultures' way to meet their primary energy demands and the second one represents the modern world's way to meet their primary energy demands. Similar conditions exist if the other needs are compared like transportation, goods, communication and other services. A difference between early people and the modern world is "population." As the population increases, the amount of energy needed gets higher.

Energy sources bring comfort to people by their use to manufacture usable products, provide air conditioning, and make peoples' lives easier with faster transportation. This feature of energy makes it a necessity for people as no one wants to lose the good things brought by energy sources. It could be possible to say "People are dependent upon energy brought to them by another source" which is primarily electrical energy. Electrical energy is easy to convert to another energy type and easier to transport than other types of energy. The most important example to show how people are dependent on electricity is the Northeast Blackout in the USA and Canada on August 14, 2003. This very large power outage caused significant problems and hardships among the people without electricity and transportation.

Today the most important energy type is electrical energy and people are primarily focusing on how to generate electricity. The basic principle to generate electricity is to first produce shaft work, and then use this shaft work to drive a generator. To obtain shaft work, there is a need for an energy conversion system.

According to International Energy Agency's 2008 report [2], oil is the most used primary energy source with 33.1% and it is followed by coal with 27.0% and natural gas with 21.1%. The principle method for using coal and oil to produce electricity is the same, which is the

Rankine cycle. The operating principle for the Rankine cycle is to heat high pressure liquid water to a superheated vapor level and use it to drive a steam turbine. The steam turbine's shaft is connected to a generator to produce electricity. The used liquid-steam mixture, having a low pressure, leaves the turbine and is cooled down in the condenser to complete the cycle.

Using natural gas to produce electricity is different from using coal and oil. In order to obtain electrical power from natural gas, a Brayton cycle is used. A Brayton cycle use air as the working fluid while the Rankine cycle uses water. Ambient air is compressed by a compressor which causes the air's temperature and pressure to increase. Then the pressurized air comes to the combustion chamber. In the combustion chamber natural gas is injected and burned. As natural gas is burned the working fluid's temperature gets higher. One of the main differences between the Brayton and Rankine cycle during heating of the working fluid is whether the working fluid and combustion gases are mixed. In the Brayton cycle combustion gases are mixed with air. Air mixed with combustion gases leaves the combustion chamber and drives a gas turbine to generate electricity. The very hot exhaust gases from the Brayton cycle are released to the atmosphere. In a combined cycle, the hot exhaust gas is used for generating superheated steam by a heat exchanger called a heat recovery steam generator (HRSG). The steam produced is used to drive a steam turbine to produce extra electricity.

Combined cycle power plants are currently popular. Natural gas has a lower cost than oil. If natural gas is compared with coal, natural gas is cleaner in terms of exhaust gases. Also natural gas power plants are easily manufactured, and have shorter start-up shut-down periods. For a 1000 MW power plant, the installation cost of a coal fired power plant is 1000 \$/kW but is only 350 \$/kW for a combined cycle power plant [1].

Although the three different primary energy sources coal, oil and natural gases are used widely throughout the world to meet people's energy demands, all three energy sources have two common negative impacts on the world: air pollution and global warming. Especially low quality coal characterized by a lower heating value produces many harmful gases like SO_2 , SO_3 , and H_2SO_4 . Oil also produces harmful gases. Natural gas is cleaner than oil and coal, but it has also harmful effects on environment, including climate change.

It is important to mention that these three energy sources are not only used to generate electricity. Coal, oil, and natural gas are also used for heating purposes.

Heating purposes can be for air conditioning purposes or for industrial process purposes. Oil has extensive usage beyond electricity production. Oil is used as the fuel for the internal combustion engines used to power almost all transportation vehicles.

One of the most negative impacts of the combustion of fossil fuels is the production of CO_2 , which is the major greenhouse gas. This greenhouse gas causes global warming and climate change. For atmospheric CO_2 the amount is measured by particles per million (ppm). The critical value for CO_2 is 350 ppm, above which unpredictable changes in the climate may be caused. The amount of CO_2 in the atmosphere has been in excess of 350 ppm since 1988 [2].

Figure 1.1 shows CO_2 emissions by year in terms of Gt [2]. It can be observed that the amount of CO_2 emitted increased significantly after the 1950s. So while the three main primary

energy sources used now, which are oil, natural gas and coal, brings significant comfort to people, they are also causing global problems due to CO_2 emissions, climate change and global warming.

The fatal characteristic of these three main primary energy sources led people to think about alternative ways to generate electricity. The most common alternative ways to generate electricity are hydroelectric energy, nuclear energy, wind energy, geothermal energy and solar energy.



Figure 1.1 CO_2 Emissions by Year [2]

Hydroelectric power is usable on rivers in which a large amount of water is trapped by a dam and when electricity is demanded the trapped water is released through channels through the dam. As water pass through the channels, its potential energy is converted into kinetic energy that drives a turbine to generate electricity. Hydraulic power plants are carbon-free but have other environmental effects. Nuclear energy is used widely all over the world. The principle is similar to conventional steam power plants but the primary energy source is nuclear fusion of an atom's nucleus rather than combustion. The reaction takes place in a reactor. Although nuclear energy seems a clean energy it has significant risks. Especially after the nuclear disaster in Fukushima, Japan, on March 11, 2011, many countries started to reconsider their future plans about nuclear power plants. Wind energy is one of the most mature clean energy applications. Geothermal energy is also known as a clean energy source. This type of energy is obtained by using hot water/steam trapped in the earth to drive a heat engine. Geothermal energy is also used for space heating applications.

The main topic of this work is solar energy. Solar energy has been used for various purposes in the past. One of the first known application was in drying for preserving food, which is still a common application.

In 1912, the world's largest solar powered pumping plant to date was built by Frank Shuman and the system was placed in Meadi, Egypt. This system is shown in Figure 1.2 [4].

The plant used parabolic troughs to focus the sun's rays onto an absorber. The solar engine had a maximum capacity of 45 kW. The plant was shut down in 1915 because of World War I and also cheap fuel prices [3].

The discovery of the photovoltaic (PV) effect in certain silicon based materials in 1839 by Becquerel [5] and the development in solar cells are milestones for electricity generation by solar energy and led solar energy to be commercialized on a broader scale.

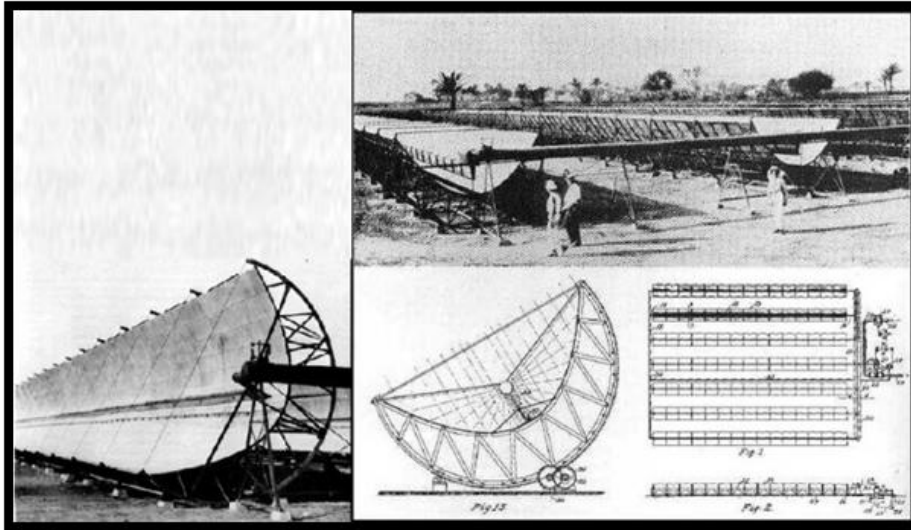


Figure 1.2 First Solar Thermal Facility in Egypt [4]

According to the International Energy Agency, Figure 1.3 shows the main sources of carbon emissions in 2008 [2]. In Figure 1.3, "Other" represents commercial/public services, agriculture/forestry, fishing, energy industries other than electricity and heat generation, and other emissions not specified elsewhere. Today, solar energy technologies can serve many of these demands to reduce carbon emission problems.

There are many areas beside electricity production where solar energy can be used efficiently. Solar Thermal energy has been used for water heating in houses for years. Flat plate collectors provide cheap and efficient solar energy utilization in sunny climates, especially in the summer. Also in some applications, solar thermal water heating is used for low temperature space heating applications together with good insulation in buildings. Without using any active heating devices, an appropriately designed building can itself provide sufficient heating using only solar energy. Trombe wall designed specific to the building is a popular method of passive solar heating technology. Utilizing solar energy is possible for other purposes like drying food, which can reduce 10-40% of the food produced that is lost due to spoilage, waste or cannot reach to the consumers [6]. Drying can serve as a good alternative to avoid food losses while transporting. Solar dryers are available in the market for this purpose. The world's hottest; most arid areas also have the highest solar radiation. This property makes solar energy available for water desalination purposes.

If solar electricity is analyzed, two basic energy conversion technologies are available: solar thermal and PV. PV involves the direct conversion of solar radiation into electricity using semi-conductors. PV does not use a heat engine to convert heat into work, and therefore PV is not a solar thermal technology. The focus of the present work is solar thermal electricity.

Solar thermal power systems are old applications for utilizing solar energy. These systems were used for melting metals in the past [7]. The early applications were small having capacities up to 100 kW and used generally for small scale applications like water pumping. Today, solar thermal power systems are used for large scaled electricity production applications in the hundreds of mega-watts range.

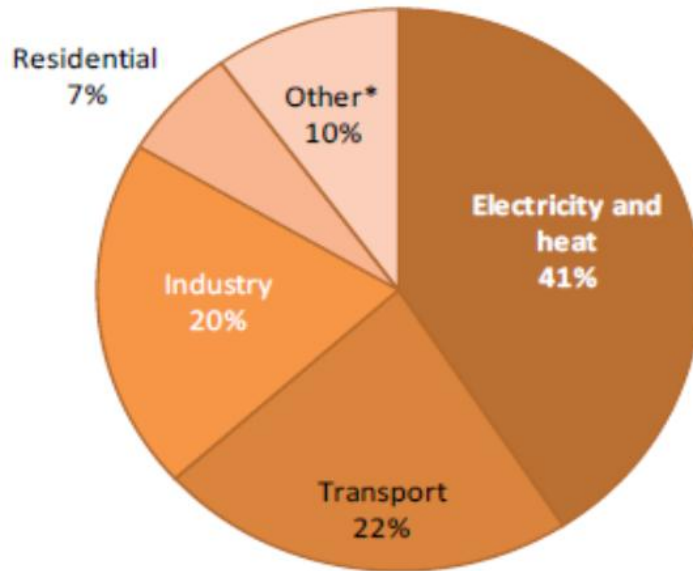


Figure 1.3 Main Sources of Carbon Emissions in 2008 [2]

Solar thermal power plants use solar collectors to drive a heat engine just like other thermal power plants using oil, coal or natural gas as mentioned in the above paragraphs.

In solar thermal power systems, solar energy is concentrated by concentrating solar collectors. With concentration, solar radiation coming to a large surface is focused on a small receiver surface to reach high temperatures. Relative to PV systems which use both beam and diffuse solar radiation, a disadvantage of concentrating solar thermal energy is that the collectors only concentrate solar beam radiation, and these systems cannot utilize the diffuse solar radiation scattered by the atmosphere.

There are several types of concentrating solar thermal power systems available. These are power tower systems, parabolic dish engine systems, parabolic trough collector systems and Fresnel systems.

1.2. Literature Review

1.2.1. Principles of CSP Technologies

In order to define the main principles of Concentrating Solar Power (CSP) technology, it is required to explain the difference between beam radiation and diffuse radiation. Some of the solar radiation received from the sun is scattered by the atmosphere. This makes some of the solar radiation rays to change their direction as shown in Figure 1.4. This is called diffuse radiation. Solar radiation that is not scattered by the atmosphere is called beam (or direct) radiation.

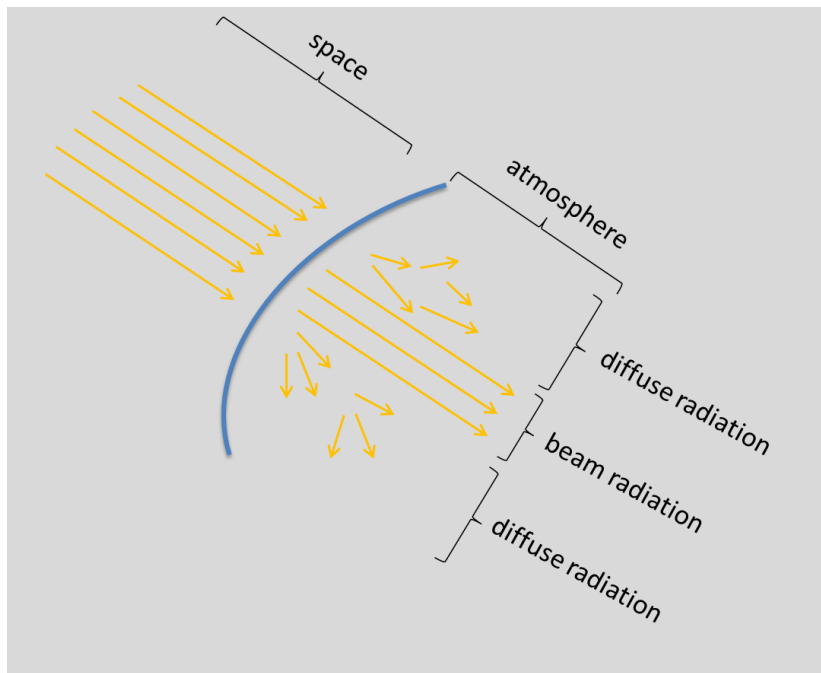


Figure 1.4 Diffuse and Beam Radiation

The area where the solar radiation is incident on is called the aperture area of a Parabolic Trough Collector (PTC), and the total area of the absorber/receiver is called the receiver area as shown in Figure 1.5.

CSP technologies can only use the beam part of solar radiation since concentration needs parallel rays. In contrast, flat plate collectors utilize both beam and diffuse radiation. Although

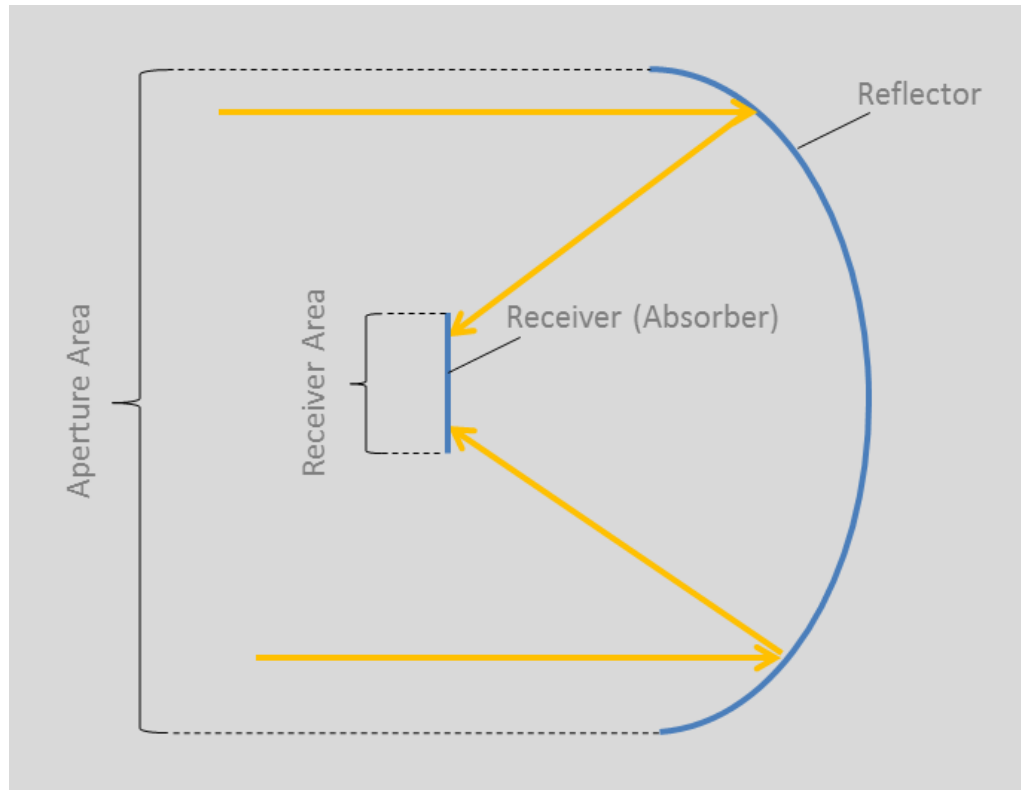


Figure 1.5 Receiver and Aperture Area of a PTC

CSP cannot utilize diffuse radiation, its main advantage over non-concentrating collectors is focusing the radiation on a specified point which can lead to high temperatures. This advantage enables CSP technologies to collect solar radiation from a large area (aperture) onto a small area (receiver). The ratio of aperture area to the receiver area is called the Concentration Ratio. Higher concentration ratio means that a larger amount of solar radiation coming to a large area is concentrated to a receiver which has a low surface area. Since the surface area on which solar radiation is absorbed is lower in CSP than flat plate collectors, heat losses per unit aperture area are lower. As a result, CSP enables higher temperatures than flat plate collectors.

There are different types of collecting principles available to concentrate solar radiation onto a receiver. These collecting principles can be grouped into two as line focusing and point focusing. Parabolic trough and Fresnel type collectors are line focusing technologies. Parabolic dish and solar power tower (or Central Receiver System) are point focusing technologies.

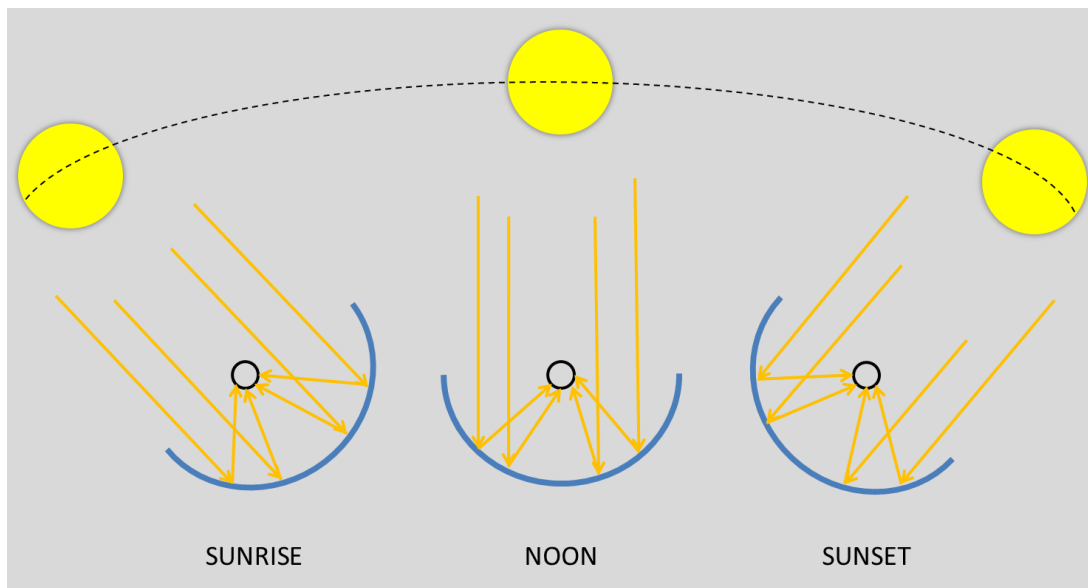


Figure1.6 Tracking in a CSP Collector

Since CSP technology concentrate the beam radiation part of solar energy, all CSP technologies need to track the sun throughout the day as shown in Figure 1.6. Line focusing CSP technologies have one axis tracking systems and point focusing CSP technologies have two axis tracking systems.

Table 1.1 shows the main characteristics of the four main CSP technologies. Detailed information for each technology will be given in the following sections.

Table 1.1 Properties of CSP Technologies available [7]

	Focusing Type	Tracking Axis	Concentration Ratio	Temperature Range (°C)
Linear Fresnel	Line	1 axis	10-40	60-250
Parabolic Trough	Line	1 axis	10-85	60-400
Parabolic Dish	Point	2 axis	600-2000	100-1500
Solar Tower	Point	2 axis	300-1500	150-2000

1.2.2. Solar Power Tower

A power tower (or central receiver) system shown in Figure 1.7 [8] uses two axis tracking mirrors to reflect and concentrate solar energy to a receiver located on a tower. These systems typically use thousands of 2 axis sun tracking mirrors called 'heliostats'. Heliostats are flat rectangular shaped mirrors.

Solar radiation is concentrated to the receiver at the top of the tower. Concentration ratios range from 300 to 1500 which leads to temperatures from 150°C to over 2000°C [7]. At the receiver, solar energy concentrated by the heliostats is absorbed by a working fluid and used to drive a heat engine to generate electricity. The heat transfer fluids used in power towers are water-steam, liquid sodium or molten salt. Power towers are generally used with Rankine cycles, but Brayton cycles are possible. Also, investigations exist for using with combined cycles [9].



Figure 1.7 Solar Power Tower [8]

The heliostat field is important for a solar tower power plant and represents approximately 50% of total cost. Additionally, the heliostat field layout causes approximately 40% of power loss [10]. Heliostat field design is a vital part of solar tower power plants. Different configurations for heliostat field layouts are being simulated to increase the efficiency of solar power tower plants.

The first commercial sized test of a solar power tower plant was “Solar One”. That project was a demonstration project located near Barstow, California. Solar One consisted of 1818 heliostats and produced 100 MWe for 8 hours in the summer and 10 MWe for 4 hours in winter. The system had water/steam as the working fluid, and operated from 1982 to 1986. Solar One was important to prove that large scale solar power tower technology is feasible. This Solar One project continued with Solar Two which was actually the extension of the existing Solar One power plant with additional heliostats. Solar Two also had 60% sodium nitrate/40% potassium nitrate molten salt as a working fluid. Molten salt provided easy heat storage for the power plant [11].

The world's first commercial solar tower power plant is the "PS10" power plant located near Seville in Spain. This power plant has a capacity of 10 MW. The PS10 power plant has 624 heliostats having a total 75,000 m² and a 100 m height tower. The power plant uses liquid water/steam as the working fluid. The PS10 power plant has a 20 MWh energy storage capacity. That heat storage enables the power plant to work 50 minutes with 50% workload of its steam turbine. Building PS10 started in 2004 it began operating in 2006 [12].

1.2.3. Parabolic Dish

Dish systems, such as that shown in Figure 1.8 [13], are parabolic mirrors which have a shape of a dish. Generally dish systems are modular and consist of a large number of relative small dishes with each dish having its own heat engine located at the focal point of the mirror. Solar energy is concentrated to each heat engine by a single parabolic mirror where heat is converted to electricity. Alternately, the heat energy collected can be transferred to a central heat engine by a number of parabolic dishes working together.



Figure 1.8 Parabolic Dish [13]

Dish engine systems have 2-axis tracking with concentration ratios of 600-2000. They can reach temperatures of 1500 °C. Dish diameter sizes range from 5 m to 25 m and have capacities ranging from 5 to 50 kW.

Dish systems having an individual heat engine generally use a Stirling engine. Despite their high cost of construction, dish systems are the most efficient concentrating solar power technologies since they are always pointing at the sun [9]. One disadvantage of the parabolic dish systems are their high cost despite their high efficiency. The high cost is due

to the high cost of the Stirling engines. Parabolic dish systems could be cost effective with decreased Stirling engine costs resulting from further research to decrease the manufacturing costs of Stirling engines. Another alternative is to use a Brayton cycle with a parabolic dish. This alternative would have lower costs but also lower efficiencies. Additionally a high capacity and efficient Brayton cycle would be too heavy and big for a parabolic dish. Finally, dish systems do not allow heat storage but solar hybridization is possible.

For a commercial size power generation, there should be a number of dishes because of their low individual capacity. Parabolic dish can be adapted for low capacity use and can be competitive with PV cells [14].

1.2.4. Fresnel

Fresnel mirrors consist of small flat optical faces. The first developer of this system is Giorgio Francia [7]. Those systems consist of long flat Fresnel mirrors with a parallel orientation as shown in Figure 1.9 [15]. Fresnel mirrors reflect sunlight to an absorbing surface. Fresnel mirrors are cheaper and have less weight compared to the parabolic trough mirrors. Fresnel systems are not commercially available now.



Figure 1.9 Fresnel Collectors [15]

1.2.5. Parabolic Trough

Parabolic trough collector (PTC) systems like that shown in Figure 1.10 [16] are the most developed systems among all concentrating solar thermal power technologies. Today most of the solar thermal power plants use parabolic trough collector systems.

Parabolic trough collector systems consist of parabolic collectors having parabolic reflective mirrors, and absorber tubes located on the focal lines of reflector arrays. Parabolic trough collector systems use a Rankine cycle to produce electricity.



Figure 1.10 Parabolic Trough Collector [16]

Existing PTC solar power plants use oil as a heat transfer fluid and heat it. Then thermal energy is transferred from the oil to water using heat exchangers. Water changes from liquid to superheated steam and drives the steam turbine. The cooled oil then flows back to the PTC to be reheated. There are researches to eliminate the heat exchanger and generate superheated steam directly in the PTC. This subject will be explained in the following chapter. For now, PTC technology is explained according to today's commercialized technology in which PTC power plants use oil as the heat transfer fluids.

PTC solar power plants works best between 40° north and south latitudes in arid or semi-arid regions. In these regions solar beam radiation is high. Like all concentrating technologies, PTC solar power plants only concentrate solar beam radiation and have concentration ratios of 70-80 [7]. Existing PTC solar power plants can heat oil up to 400°C. PTCs track the sun in one axis to concentrate beam radiation to its focal axis. PTC's are typically rotated about a north-south axis to maximize the annual power produced, although rotation about an east-west axis can maximize winter production.

PTC solar power plants are available with fuel burners in some applications to continue producing electricity when the weather is cloudy or after sunset. Also, some PTC solar power plants use heat storage units. Heat storage units are tanks filled with salt. Heat is stored as the salt in the tank melts and the stored heat is used when solar energy is not available. In order to work with heat storage units, PTC arrays are designed above the capacity of the steam turbine used in the power plant. In working hours of PTCs, heat required to generate steam to drive the steam generator is used, while the remaining heat is stored in the molten salt tanks to be used later.

PTC solar power plants are the most developed, proven and cheapest way to use solar energy to produce electricity since significant work on PTC solar power plants has been completed, including experiments and prototypes. Also PTC is currently the most commercially proven way for CSP power plants, which proves its suitability.

One of the most important reasons PTC solar power plants have been proven as a way of generating electricity is from the SEGS ('Solar Electric Generating System'). The oil crisis in the early 1970s led R&D for CSP plants and also PTC technology. Within the SEGS projects, nine commercial PTC solar power plants were built. Their capacities ranged from 14 to 80 MWe with a total capacity of 354 MWe. The nine power plants are located in Mojave Desert, California [17].

1.2.6. Direct Steam Generation in Concentrating Solar Thermal Power Plants

Today, most of the parabolic trough collector (PTC) solar power plants use oil as a heat transfer fluid (HTF) that is circulated through absorber tubes. The heated oil is used to produce steam with the use of heat exchangers. The most important factors to make solar power plants to be more commercially viable are to reduce costs and increase efficiencies. Today's PTC solar power plant's heat exchangers increase the building cost and decrease the efficiency. In order to avoid these disadvantages, new generation plants are being developed to generate steam directly in the collectors and using this steam directly in the turbine without using a heat exchanger. This method is called Direct Steam Generation (DSG).

PTC power plants using DSG have the potential for higher efficiencies and lower investment costs since there will not be heat exchangers for steam generation. Today PTC solar power plants have risks due to leaking oil causing fires such as in the one in SEGS II solar thermal power plant where the therminol tank exploded [18]. But in DSG the HTF is liquid/steam water and thus no oil is used. DSG systems are environmentally friendly and more reliable than classical PTC plants using oil as the HTF. Since oil is eliminated, the plant design will be simpler. Finally, current PTC solar power plants have a temperature limit of 400°C due to the oil, but in DSG this limit could be exceeded resulting in higher heat engine efficiencies.

DSG have also some disadvantages, such as the control system is expensive and complicated. The two-phase flow inside the heat collecting element can result in large temperature gradients, and therefore large thermal stresses. DSG needs higher mass flow rates in order to avoid stratified flow which is explained in Section 2.1.2 [3].

Historically, the first DSG collector was invented by John Ericsson. This was a 373 W collector that has never been commercially available [3].

As mentioned in the Introduction chapter, Section 1.1, in 1912, the world's largest solar powered pumping plant to date was built by Frank Shuman and the system was placed in Meadi, Egypt. The facility had a 75 kW mechanical capacity. This plant used parabolic trough collectors with direct steam generation [3]. That facility is considered as the first commercial DSG solar thermal plant.

Although the first initiatives for PTC were using direct steam generation, subsequent researches and initiatives used other HTF technologies. This was because of the problems created by the two phase flow in the absorber tube.

In order to answer some of the concerns about DSG, the DISS (DIrect Solar Steam) project was initiated and a test facility built at Plataforma Solar de Almería in Spain. This facility has a 100 m long collector array and a 2 MW capacity. Different operation alternatives were tested in this facility with different pressures. The facility was also used to test start-up and shut-down procedures and test the strain rate of the absorber tube. The facility worked more than 3500 hours from 1999 to 2001 [19].



Figure 1.11 DISS Facility [19]

Three different operation alternatives for DSG using parabolic trough collectors were tested at the DISS facility. The first operating option was once through. In once through, water passes through the absorber tube once and at the end, steam is generated. This operation mode is the simplest in terms of piping but the most complicated for the control system. In injection mode, liquid water is injected at several points along a series of collectors and liquid water is re-circulated through the collector row. In the recirculation mode, a liquid-steam separator is used at the end of the evaporating part of collectors and the liquid is re-circulated. Recirculation mode is the most secure but the most expensive method because of the separator cost [19][20].

The DISS project was a milestone for the DSG solar power plant industry because the project proved that a DSG solar power plant is feasible. The experience gained by the DISS project let the researchers design a commercial sized DSG solar power plant. The INDITEP project was initiated for that purpose. In [21], a conceptual design of INDITEP is explained. The design is for a 5 MWe DSG solar power plant. The design consists of 7 collector loops with 10 collectors for each loop. For a single loop of collectors the first 8 collectors are designed for preheating and evaporating. The final 2 collectors are for superheating. After the first 8 collectors, which is before the superheating section, there is a separator to separate liquid water and vapor. Separation is important to have fully superheated steam at the superheating section of the collector loop. There will be remaining saturated liquid water in the separator and that remaining liquid water is recirculated through the collector loop.

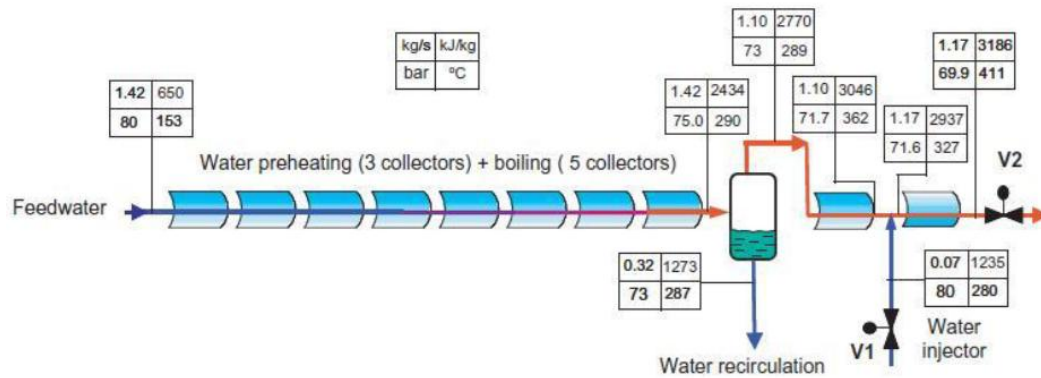


Figure 1.12 Schematic Representation of Solar Array in INDITEP Project [21]

For a power plant, it is important to produce the correct amount of electricity at the demanded time. For a steam power plant, the temperature, pressure and mass flow rate of steam entering the steam turbine should be adjusted according to the power need for that time. For a conventional steam power plant these adjustments can be done easily by simply changing the steam flow rate and changing the fuel mass flow rate. The advantage of a conventional steam power plant is that the heat source is controllable and can be changed accordingly, which is not possible for a solar thermal power plant either using HTF technology or DSG because solar radiation is never a constant value at any time. For a CSP solar thermal power plant using HTF technology, the oil flow rate through the collectors can be adjusted so that a specified temperature at the outlet of the collectors can be achieved. By a heat exchanger heat can be transferred to water to have a specified steam temperature with energy loss due to heat exchanger efficiency, and the energy loss causing the plant efficiency to be decreased. In a DSG solar thermal power plant the same control strategy cannot be adapted. For a DSG solar thermal power plant, the outlet steam temperature cannot be adjusted by changing the mass flow rate of the water through the absorber tube. When the mass flow rate of water through the boiling part of the absorber pipe is changed, the amount of saturated vapor gained by the separator will be constant. This behavior makes controlling the steam temperature at the collector outlet by only changing mass flow rate impossible for DSG collectors. In [21], a simple method is used to control outlet steam temperature. Some portion of the recirculating liquid water that is separated before the superheating section is injected before the last collector of one loop. This method makes the control of the outlet steam temperature easier.

Odeh et al [22] presented a thermal analysis of trough collectors and suggests a correlation for thermal heat losses from a trough collector that has conduction, convection and radiation components as shown in Equation 2.13. This correlation is based on absorber temperature so that the model can be applied to any working fluid for a PTC. Also in this work a mathematical model is presented for heat transfer for a DSG collector and the results are analyzed.

1.2.7. PTC Solar Thermal Power Plant Models

The performance of solar energy conversion systems is highly dependent on the place that the solar facility is installed due to significant spatial variations in solar resources. For testing a solar facility's performance, simulation programs are used in order to avoid high installation costs. Simulation programs make it easier to predict a solar energy system's performance.

Ho made research about simulation programs used to simulate concentrating solar power (CSP) technologies for Sandia National Laboratories [23]. That work explains briefly different simulation programs and separates them according to different CSP technologies.

Several researchers were interested in simulating SEGS VI power plants. The reason is that real data are available for a working solar thermal power plant using HTF technology with parabolic trough collectors. That property gave people the opportunity to compare their simulation results with real operating data. Comparing with real data is important to prove if the model is correct and determine how accurate the results are.

Different researchers use different simulation environments to simulate the SEGS VI power plant. Using EASY software Lippke modeled the SEGS VI power plant first in 1995 [24]. Lippke's work is continued by Jones at al. [25] and Patnode [26]. Jones at al used TRNSYS for the entire simulation but Patnode used TRNSYS and EES (Engineering Equation Solver) together.

Usta made a TRNSYS simulation of the SEGS VI power plant and good agreement was found between the existing literature about the same power plant and predicted results. Usta then ran the model using Antalya's meteorological data [27].

1.2.8. Thesis Objective

In [21] a DSG solar power plant is simulated and the results for specified inlet conditions are presented, but the underlying theory is not presented including the control strategy. In [22], a DSG collector model is presented but it does not show the behavior of a DSG solar collector array or a power plant working with DSG technology. The objective of this thesis is to model and simulate a DSG collector array and a CSP solar power plant using DSG technology while presenting the underlying theory in the literature for both. In this thesis a DSG model is presented which is based on [22] and a power plant model is presented based on [21]. This thesis is unique in that both the underlying theory for modeling a DSG solar collector array and simulation results together will be summarized.

CHAPTER 2

DSG MODELING

2.1 Collector Model

2.1.1 Solar Resources

As mentioned in Chapter 1, CSP technologies need to track the sun to focus solar beam radiation onto a receiver. The direction of the reflector surface should be arranged according to the position of the sun at each instant in time. If the sun is not tracked or the tracking is not accurate, the solar radiation is not focused on the absorber surface which means zero collector efficiency. This section is about the solar geometry that a CSP solar collector should rely on. The geometric relationship between a plane and solar beam radiation are described here in terms of several angles. The angles are described in Figure 2.1. The content of the Section is adapted from [28].

To describe the equations required to define the direction of solar beam radiation relative to a solar collector, the angles shown in the Figure 2.1 should be defined.

Latitude (ϕ) is the angular location north or south of the equator. North of the equator is positive, south is negative, and $-90^\circ \leq \phi \leq 90^\circ$.

Declination angle (δ) is the angular position of the sun at solar noon on the current day relative to that on the equinox.

Slope (β), is the angle between the collector and the horizontal surface (earth), $0^\circ \leq \beta \leq 180^\circ$.

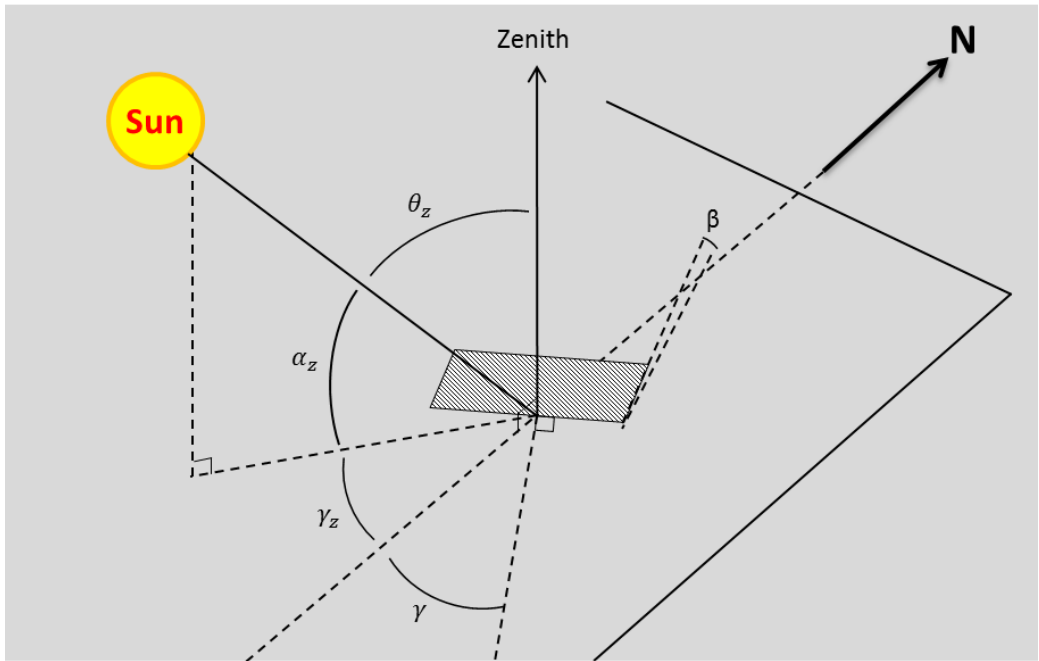


Figure 2.1 Solar Angles

Surface azimuth angle (γ) is the deviation of the projection on a horizontal plane of the normal to the surface from the local meridian, with zero being due south, east negative and west positive, $180^\circ \leq \gamma \leq 180^\circ$.

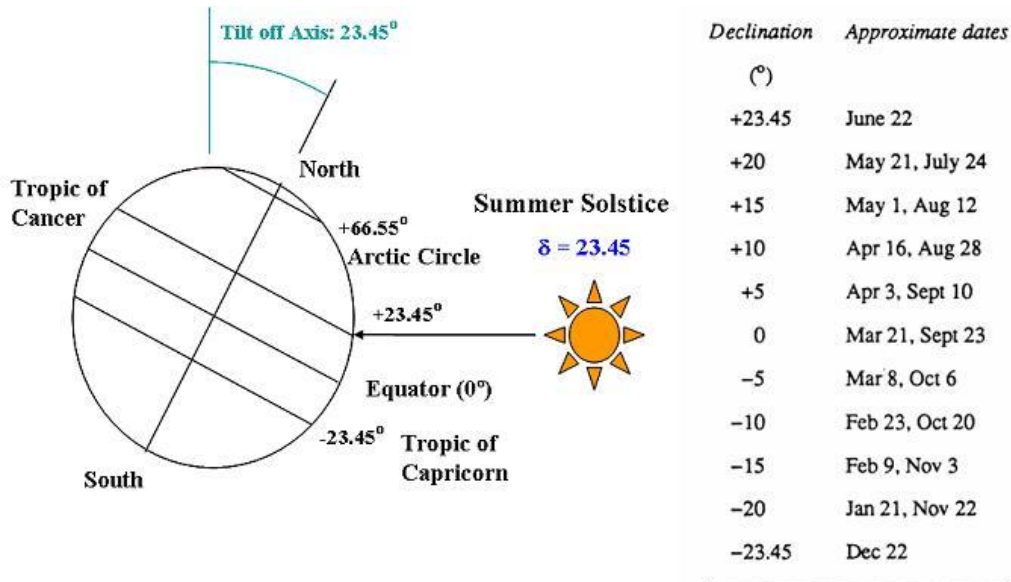


Figure 2.2 Declination Angle [28]

Hour angle (ω) is the angular displacement of the sun east or west of the local meridian due to rotation of the earth about its axis at 15° per hour; morning is negative, and afternoon is positive.

Angle of incidence (θ) is the angle between the beam radiation on a surface (collector) and the normal to that surface.

Zenith angle (θ_z) is the angle between the vertical and the line to the sun. This angle is equal to the angle of incidence for a horizontal surface. Angle of incidence and zenith angles are shown in Figure 2.3.

The declination angle (δ) is calculated in [28] as,

$$\delta = 23.45 \sin\left(360 \frac{284+n}{365}\right) \quad (2.1)$$

where n is the day number of the year.

Declination angles for approximate dates and the summer solstice schematic are shown in Figure 2.2 [29].

The angle of incidence of beam radiation on a collector surface is calculated as,

$$\begin{aligned} \cos \theta = & \sin \delta \sin \phi \cos \beta - \sin \delta \cos \phi \sin \beta \cos \gamma + \\ & \cos \delta \cos \phi \cos \beta \cos \omega + \cos \delta \sin \phi \sin \beta \cos \gamma \cos \omega + \cos \delta \sin \beta \sin \gamma \sin \omega \end{aligned} \quad (2.2)$$

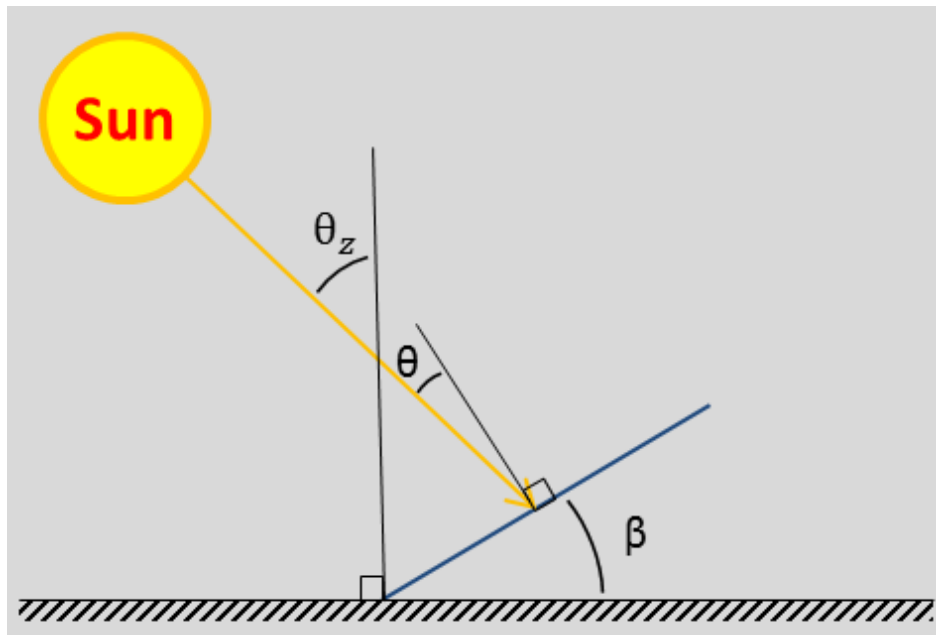


Figure 2.3 Angle of Incidence and Zenith Angle

For a horizontal surface, $\beta=0^\circ$, and in this case the angle of incident becomes equal to zenith angle,

$$\cos \theta_z = \cos \phi \cos \delta \cos \omega + \sin \phi \sin \delta \quad (2.3)$$

Equations (2.2) and (2.3) with θ substituted for θ_z are for tilted and horizontal stationary surfaces (collectors), respectively. The scope of this thesis is parabolic trough collectors which are tracking the sun on one axis continuously in order to focus solar radiation to the absorber. There are two different alternatives for a PTC solar array in terms of tracking axis. One with tracking about a N-S axis (North-South Axis Tracking) and the other with tracking about an E-W Axis (East-West Axis Tracking). Figure 2.4 shows the schematic for the orientation of both tracking options.

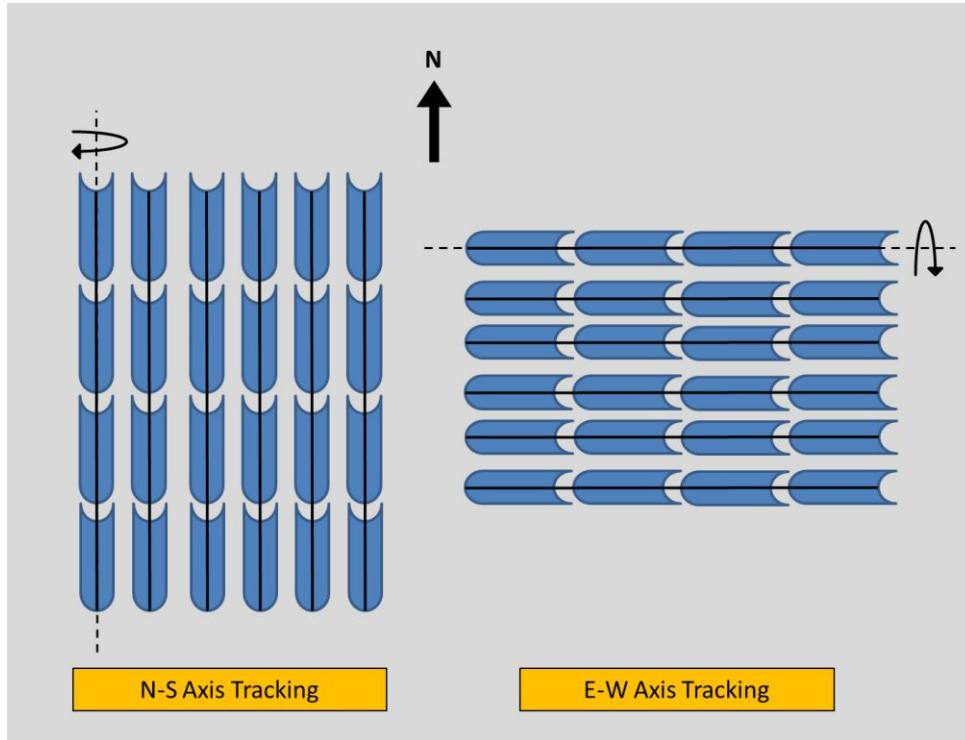


Figure 2.4 N-S and E-W Axis Tracking

For a solar collector array rotated about a North-South axis with continuous adjustments, the angle of incidence is calculated as,

$$\cos \theta = (\cos^2 \theta_z + \cos^2 \delta \sin^2 \omega)^{1/2} \quad (2.4)$$

For a solar collector array rotated about an East-West axis with continuous adjustments, the angle of incidence is calculated as,

$$\cos \theta = (1 - \cos^2 \delta \sin^2 \omega)^{1/2} \quad (2.5)$$

For point focusing collecting systems which are solar power tower and dish systems, two axis tracking is needed. For two axis tracking, the angle of incidence is minimized such that ideally,

$$\cos \theta = 1 \quad (2.6)$$

The maximum amount of solar radiation which is utilized by a concentrating solar collector is calculated as,

$$Q_{max} = DNI \cos \theta \quad (2.7)$$

As Equation 2.7 indicates, as $\cos \theta$ reaches to 1, a solar collector utilizes as much as possible from solar radiation. Two-axis tracking with continuous and perfect adjustments always gives $\cos \theta = 1$ in theory which means all DNI (direct normal irradiance) is received by the collector. However, two-axis tracking is more expensive to implement than one-axis tracking.

The angle of incidence for perfect East-West axis tracking is always zero at solar noon. The angle of incidence for perfect North-South axis tracking is minimized in the morning and evening. East-West axis tracking maximizes resources at solar noon and while North-South axis tracking maximizes resources in the morning and evening. For latitudes and meteorological conditions typical for Turkey, East-West maximizes winter resources while North-South maximizes summer and annual resources. As a result, most of the PTC solar thermal power plants are North-South oriented.

In solar energy, two different types of time definitions exist. Solar time is calculated according to the sun's position relative to the local meridian on earth. Standard time is based on the time zone that one place belongs to. Conversion between solar time and standard time is calculated as,

$$\text{Solar Time} - \text{Standard Time} = 4(L_{st} - L_{loc}) + E \quad (2.8)$$

where;

L_{st} = Standard meridian for the local time zone [degrees]

L_{loc} = The longitude of the location [degrees]

E = The equation of time [min]

The equation of time is calculated as,

$$E = 229.2(0.000075 + 0.001868 \cos(B) - 0.032077 \sin(B) - 0.014615 \cos(2B) - 0.04089 \sin(2B)) \quad (2.9)$$

Where;

$$B = \frac{360}{365}(n - 1) \text{ [degrees]} \quad (2.10)$$

A study has been done for a collector, which uses Antalya's geographical data ($\phi = N 36^\circ 53'$), assuming that there is no atmosphere and extraterrestrial radiation equal to solar constant (G_{sc}) is coming to earth.

$$G_{sc} = 1367 \text{ W/m}^2 \quad (2.11)$$

Using Equation 2.7, a computer code was developed to calculate average daily solar radiation coming to the tracking surfaces per m^2 for each month of the year. Results are shown in Figure 2.5. In Figure 2.5 E-W represent the east-west axis and N-S represents north-south axis tracking.

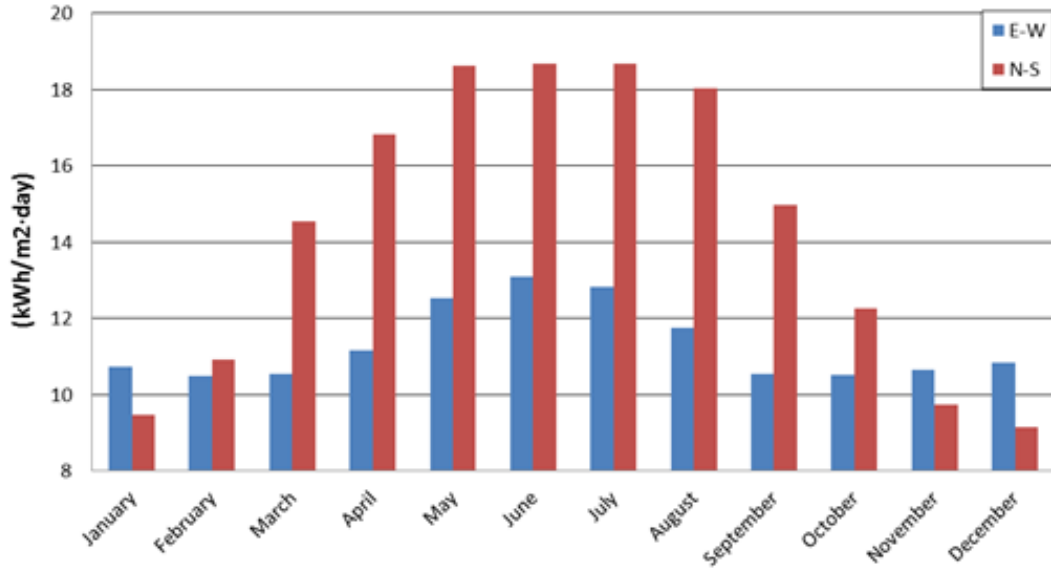


Figure 2.5 Comparisons of N-S and E-W Axis Tracking by Month

In addition to losses due to the angle of incidence there are other losses which occur due to additional absorption and reflection losses as the incident angle is increased. In order to calculate these losses a model for an incident angle modifier (IAM) proposed by Dudley et al. [26] is used.

$$IAM = 1 + 0.000884 \frac{\theta}{\cos\theta} - 0.00005369 \frac{\theta^2}{\cos\theta} \quad (2.12)$$

Where θ is in degrees.

2.1.2 Flow In a DSG Collector

Two phase flow is an important phenomenon and issue throughout the energy industry. Two-phase flow means two different phases of fluids that are flowing in the same medium. Generally these two phases are liquid and gas. For DSG in a PTC, water and steam are flowing through a steel pipe.

In order to explain the flow characteristics for a DSG collector, general information about two phase flow in a horizontal pipe should be given.

Two phase flow can behave in different regimes in a pipe. The primary factors affecting the regime of two phase flow in a pipe are flow rate and quality. Flow patterns possible for two phase flow through a horizontal pipe are shown in Figure 2.6.

Bubbly flow refers to two phase flow with a low quality and high mass flow rate. Bubbles are formed and dispersed at the top of the pipe due to their buoyancy.

For lower flow rates, complete separation between the two phases occurs which is called Stratified Flow.

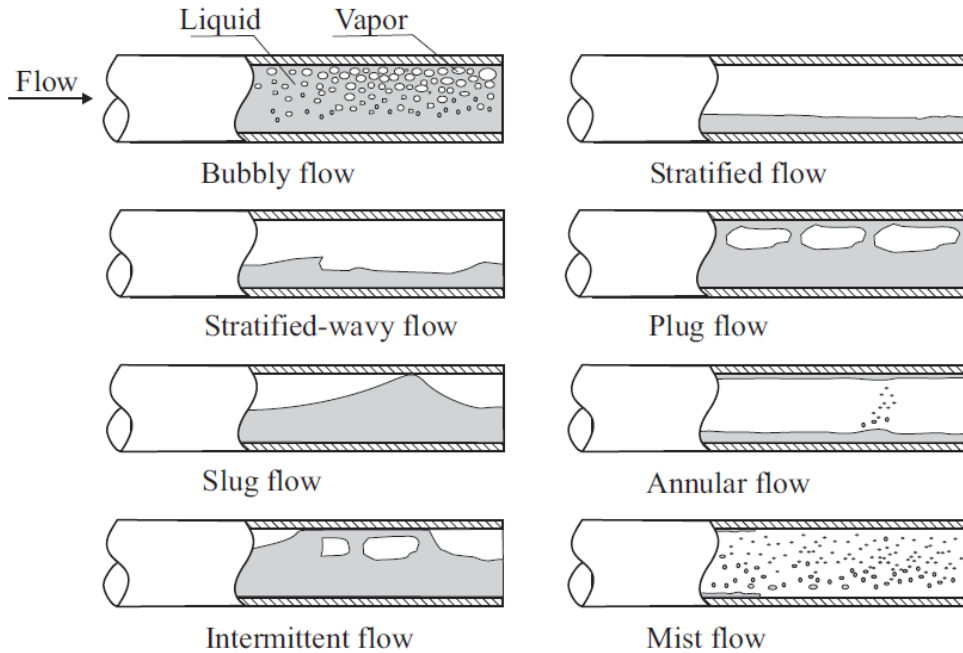


Figure 2.6 Two Phase Flow Regimes [33]

If the velocity of the gas phase is increased in a stratified flow regime, waves are formed in the liquid phase of the flow. But the crest of the waves does not reach the top of the tube. This flow regime is called Stratified Wavy Flow. Waves are occurring due to the friction between the gas and liquid.

If the gas velocity is increased further than the Stratified Wavy flow, waves can reach the top of the tube. This flow regime is called Intermittent Flow. Two categories of Intermittent Flow exist. The Plug Flow regime has liquid plugs separated by elongated bubbles. The bubbles are relatively smaller than the tube diameter. Slug Flow occurs when the gas velocity is further increased. In Slug Flow, bubbles are elongated through the tube and the length of the bubbles are on the order of the diameter of the tube.

For high quality and high velocity flow, Annular Flow occurs where the cross section of the tube looks like an annulus. Gas flow occurs at the core of the annulus and the liquid phase of the flow occurs at the crust of the annulus.

At higher velocities than annular flow, the liquid phase of the flow appears as bubbles in the gas flow. This flow regime is called Mist Flow.

Odeh et al. [22] proposed a DSG model on which this thesis' DSG model is based. Odeh et al.'s model is based on the assumption that the incident energy input is uniform for the entire length of the absorber.

Assuming that single phase water is entering the collector, the temperature of the water increases in the flow wise direction to the saturation temperature. After that point, as shown in Figure 2.6, bubble formation begins and nucleate boiling starts, and in this case the flow regime is bubbly flow. As the quality of the flow is increased, the heat transfer rate is increased. The reason for the increase in heat transfer rate is the shear stress of the bubbles inside the absorber tube. As the quality of the flow is increased, the flow regime becomes Intermittent and further increases in the quality results as annular flow regime. Assuming that the flow rate is high, the annular flow regime dominates in a DSG collector.

Figure 2.7 shows the flow regime representation of a horizontal tube heated by a uniform heat flux as in a DSG solar PTC.

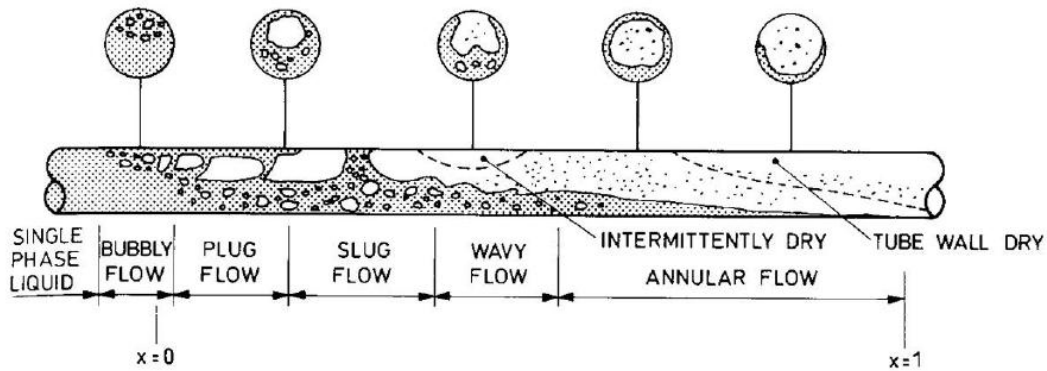


Figure 2. 7 Two Phase Flow in a Horizontal Tube [22]

2.1.3 Heat Losses

For the PTC absorber shown in Figure 2.8, the absorber is made of a steel tube. The steel absorber tube is covered by an absorber surface coating which is generally cermet or black chrome. Around the absorber tube, there is a glass envelope. The space between the absorber and the glass envelope is evacuated.

Heat losses from the absorber tube can be via radiation to the glass envelope and by conduction due to residual gases in the evacuated space. In addition, some heat losses occur via vacuum bellows and supports that occur periodically along the absorber tube.

Heat losses from the glass envelope of the absorber can occur via radiation to the sky and convection to the surrounding.

In [22], a correlation is proposed in order to calculate thermal heat losses from an absorber of a DSG solar PTC. This correlation is generated by [22]. The authors developed a fairly complex model of the PTC using 16 equations based on first principles and ran many parametric studies in which wind speed, absorber temperature, ambient temperature, and DNI were varied. The authors then curve fit this simplified semi-empirical correlation to the results from the parametric study to arrive at a simplified model. The model representing all heat losses mentioned above in terms of absorber temperature and ambient temperature.

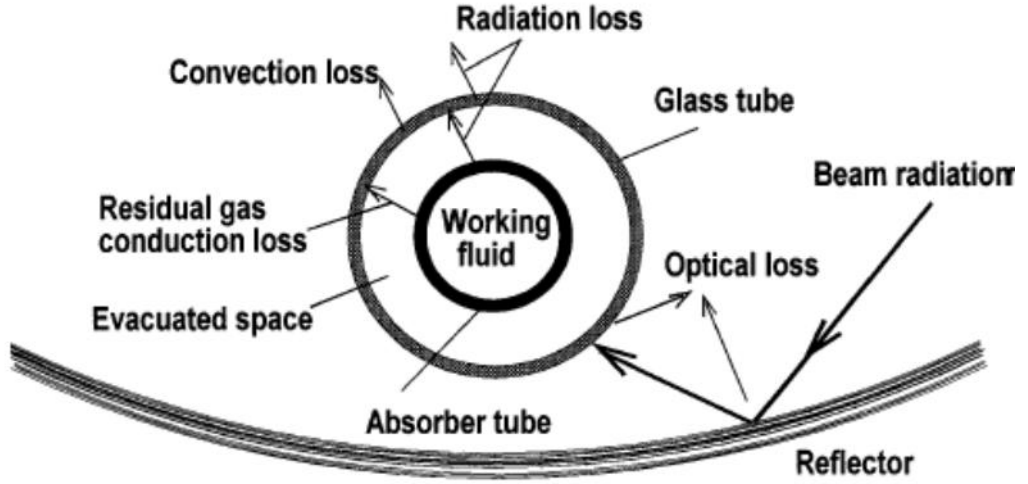


Figure 2. 8 Thermal and Optical Losses on Absorber Tube [22]

$$Q_{loss,thermal} = (a + cV)(T_{ab} - T_{amb}) + \epsilon_{ab}b(T_{ab}^4 - T_{sky}^4) \quad (2.13)$$

In Equation 2.13, V is the wind speed in m/s. For the absorber used in this thesis, which has an inner diameter of 55 mm and outer diameter of 70 mm,

$$a = 1.91 \times 10^{-2} \text{ WK}^{-1}\text{m}^{-2} \quad (2.14)$$

$$b = 2.02 \times 10^{-9} \text{ WK}^{-4}\text{m}^{-2} \quad (2.15)$$

$$c = 6.608 \times 10^{-3} \text{ JK}^{-1}\text{m}^{-3} \quad (2.16)$$

Where parameter a is for conduction, b is for radiation and c is for convection heat losses. Equation 2.13 is generated in [22] by curve fitting all types of heat losses mentioned in order to generate Equation 2.13. The sky temperature is found as follows,

$$T_{sky} = (\epsilon_{sky})^{0.25} T_{amb} \quad (2.17)$$

$$\epsilon_{sky} = 0.711 + 0.56(T_{dp}/100) + 0.73 (T_{dp}/100)^2 \quad (2.18)$$

In Equation 2.17, T_{amb} is the ambient temperature. In Equation 2.18, T_{dp} is the dew point temperature.

In Equation 2.13, ϵ_{ab} is the emissivity of the absorber. In this work absorber surface is assumed to be coated with cermet material. The emissivity of cermet coating is calculated as [22],

$$\epsilon_{ab} = 0.00042T_{ab} - 0.0995 \quad (2.19)$$

Where, T_{ab} is in Kelvin.

In addition to the thermal losses, there are optical losses due to absorber glass envelope and reflector surface. The total optical efficiency in the model is assumed as 0.74 based on [21].

$$Q_{loss,optical} = (1 - 0.74)Q_{max} \quad (2.20)$$

The net energy gained by the absorber is calculated as,

$$Q_{net} = Q_{max} - (Q_{loss,thermal} + Q_{loss,optical}) \quad (2.21)$$

2.1.4 Heat Transfer to the Working Fluid

In order to explain the heat transfer to the working fluid in a DSG solar PTC, the thermal analysis should be divided into two different sections. One part of the analysis should treat the one phase flow which consists of liquid water and dry steam. The second part should treat the two-phase flow where the heat transfer characteristic of the flow is changing.

For the one phase part of the flow, the convective heat transfer coefficient is found from the Dittus-Boelter correlation,

$$h_{1ph} = 0.023(Re)^{0.8}(Pr)^{0.4} \frac{k}{D_{ab,i}} \quad (2.22)$$

In order to evaluate the convective heat transfer coefficient for the two phase flow, the flow regime should be determined. In a DSG solar PTC collector, there are two alternatives for the flow regime. One alternative is stratified flow, the other alternative is annular flow. In order to determine whether the flow is stratified or annular, the Froude number should be calculated [22]. The Froude number is the ratio of the inertia forces to the gravitational forces.

$$Fr = \frac{G^2}{\rho_l^2 \cdot g \cdot D_{ab,i}} \quad (2.23)$$

If $Fr < 0.04$, stratified flow occurs in the absorber tube, and in this case, the convective heat transfer coefficient for two phase flow is calculated with the Shah equation as,

$$\frac{h_{2ph}}{h_l} = 3.9(Fr)^{0.24} \left(\frac{x}{1-x}\right)^{0.64} \left(\frac{\rho_l}{\rho_g}\right)^{0.4} \quad (2.24)$$

The heat transfer coefficient for the liquid phase only is found assuming the liquid phase of the working fluid is filling the tube. In this case the Dittus-Boelter equation becomes,

$$h_l = 0.023 \left(\frac{k_l}{D_{ab,i}} \right) \left(\frac{G(1-x)D_{ab,i}}{\mu_l} \right)^{0.8} (Pr_l)^{0.4} \quad (2.25)$$

If, $Fr > 0.04$ annular flow occurs, and in this case the Chan correlation [22] is used to determine convective heat transfer coefficient for two phase flow. The Chan correlation calculates the convective heat transfer coefficient as the sum of two different coefficients. The two components are bubble formation and convection.

$$h_{2ph} = h'_b + h'_l \quad (2.26)$$

The convection component of the heat transfer coefficient is found as follows,

$$h'_l = h_l F \quad (2.27)$$

Where F is the enhancement factor, and found as,

$$F = 1 + (2.4 \times 10^4)(Bo)^{1.16} + 1.37(X_{tt})^{-0.86} \quad (2.28)$$

X_{tt} is the Martinelli parameter, found as,

$$X_{tt} = \left(\frac{\rho_g}{\rho_l} \right)^{0.5} \left(\frac{\mu_l}{\mu_g} \right)^{0.1} \left(\frac{1-x}{x} \right)^{0.9} \quad (2.29)$$

Bo is the boiling number which is calculated as,

$$Bo = \frac{q}{\dot{m} h_{fg}} \quad (2.30)$$

Here, q is the heat flux.

The bubble formation component of the heat transfer coefficient is found as follows,

$$h'_b = h_B S \quad (2.31)$$

where, S is called the correction factor.

$$h_B = 3800 \left[\frac{q}{20000} \right]^n F_p \quad (2.32)$$

Where q is the heat flux in terms of W/m^2

$$n = 0.9 - 0.3(P_n)^{0.15} \quad (2.33)$$

$$F_p = 2.55(P_n)^{0.27} \left(9 + \frac{1}{1-P_n^2} \right) P_n^2 \quad (2.34)$$

$$P_n = P/P_{cr} \quad (2.35)$$

Here, P is the working pressure and P_{cr} the critical pressure in terms of bars. The critical pressure for water is 221 bars.

The correction factor is calculated as,

$$S = 1/[1 + (1.15 \times 10^{-6})(F)^2(Re)^{1.17}] \quad (2.36)$$

The Reynolds number is calculated as,

$$Re = \frac{G(1-x)D_{ab,i}}{\mu_l} \quad (2.37)$$

In this model, heat transfer to the working fluid is calculated under the assumption of constant outer surface temperature (T_{ab}). The model is flow in a cylinder with constant surface temperature. With this assumption, the overall heat transfer coefficient is calculated as [30],

$$U = \frac{1}{\frac{1}{h} + \frac{r_i}{k} \ln \frac{r_o}{r_i}} \quad (2.38)$$

In Equation 2.38, U is the overall heat transfer coefficient, r_i and r_o are inside and outer radiuses respectively. h Is the convection heat transfer coefficient, which is calculated according to the state of the fluid described above.

In Equation 2.38, k is the thermal conductivity of the pipe material. In this model pipe material is taken as AISI 304 stainless steel. In the model, thermal conductivity of the pipe material is calculated using the reference values taken from [30] as shown in Table 2.1.

Table 2.1 Thermal Conductivity of AISI 304 Steel

T (K)	k (W/mK)
300	14,9
400	16,6
600	19,8
800	22,6

As shown in Table 2.1 there is a 50% difference in thermal conductivity over a temperature change on the order of 500 K. In order to have more accurate results, a function is generated by curve fitting the values and a thermal conductivity function is generated as,

$$k(T) = -3 \times 10^{-9} T^3 + 10^{-6} T^2 + 0.0175 T + 9.64 \quad (2.39)$$

In Equation 2.39, T is the temperature in Kelvin.

For flow in a horizontal cylinder, if the inlet mean temperature ($T_{m,in}$) is known, the exit mean temperature ($T_{m,e}$) can be calculated using the Equation 2.40 [30].

$$\frac{T_{ab} - T_{m,e}}{T_{ab} - T_{m,in}} = \exp\left(-\frac{PL}{\dot{m}c_p}\right) \quad (2.40)$$

In Equation 2.40, P is the perimeter of the inside surface of the tube, c_p is the constant pressure specific heat of the working fluid, L is the length of the tube.

2.1.5 Pressure Drop

Pressure drop is important for a power plant to determine the pump power and as a result the internal energy requirement for the pumps used. In a DSG solar PTC, pressure drop should be calculated for one phase and two phase components separately. For the one phase pressure drop, major and minor losses should be calculated. For turbulent flow conditions major pressure drop is explained in [31] as,

$$\Delta P_{l,major} = f \frac{\bar{v}^2 L}{2 D} \rho \quad (2.41)$$

where f is the Darcy friction factor, which is a function of Reynolds number (Re) and relative roughness of pipe for turbulent flow.

The friction factor can be found by an iterative method described in [31],

$$\frac{1}{f^{0.5}} = -2.0 \log \left(\frac{e/D}{3.7} + \frac{2.51}{Re f^{0.5}} \right) \quad (2.42)$$

Since equation 2.42 is an iterative method, there is a need of an initial estimation.

$$f_0 = 0.25 \left[\log \left(\frac{e/D}{3.7} + \frac{5.74}{Re^{0.9}} \right) \right]^{-2} \quad (2.43)$$

Using Equation 2.43 as an initial estimation, a single iteration will give a 1% accurate result [31]. In Equations 2.42 and 2.43, e/D is named as the relative roughness of the pipe used in the process. To find relative roughness, Figure 2.9, is used according to the pipe diameter and pipe material.

For the minor losses, a DSG collector has 4 standard 90° elbows, and the pressure drop of the 4 elbows are calculated as

$$\Delta P_{l,minor} = f \frac{\bar{v}^2 L_e}{2 D} \rho \quad (2.44)$$

In Equation 2.44, L_e/D is the equivalent length, which is equal to 30 for 90° elbows [31].

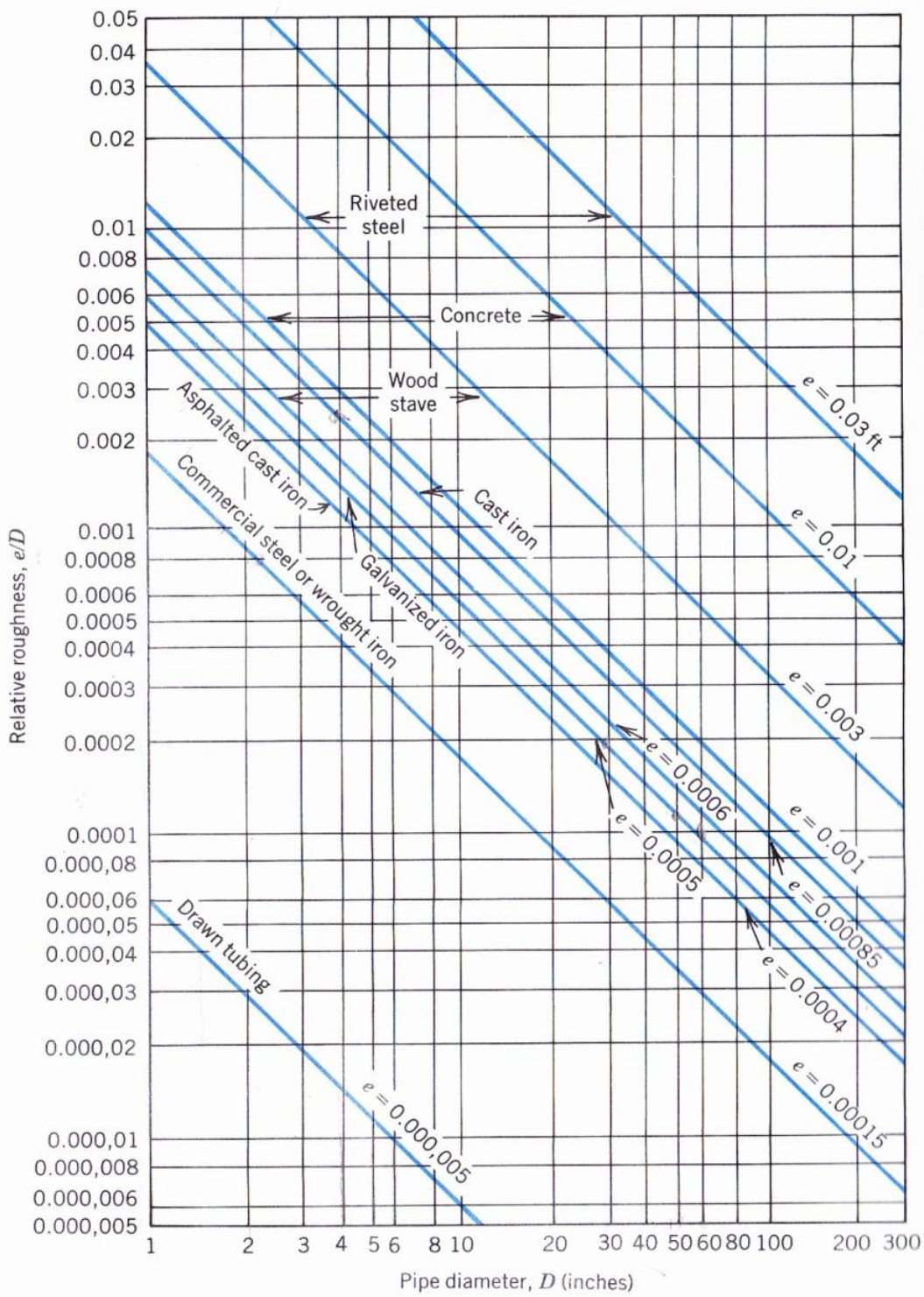


Figure 2.9 Relative Roughness versus Pipe Diameter For Different Pipe Materials [31]

For two phase flow, pressure drop calculations are presented in [32] and [33] for the following different correlations: Friedel, Lockhart and Martinelli; Grönnerad, Chisholm, Bankoff, Chalwa and Müller-Steinegen; and Heck Correlations. In this work, Friedel is chosen for the pressure drop model since the collector model presented here satisfies the requirements of this model as described in [32] as,

$$\frac{\mu_l}{\mu_g} < 1000 \quad (2.45)$$

$$G < 2000 \text{ kg/m}^2\text{s} \quad (2.46)$$

The Friedel correlation uses the two phase multiplier,

$$\Delta P_{friction} = \Delta P_l \Phi_{fr}^2 \quad (2.47)$$

Here ΔP_l is calculated using Equation 2.44 for minor pressure drop and Equation 2.41 for major pressure drop, respectively. One difference is made when calculating the friction factor.

$$f = \frac{0.079}{Re^{0.25}} \quad (2.48)$$

The two phase multiplier is found as,

$$\Phi_{fr}^2 = E + \frac{3.24 F H}{Fr_H^{0.045} We_L^{0.035}} \quad (2.49)$$

In Equation 2.49, E, F, H and We are dimensionless numbers. Fr is found by using Equation 2.23.

$$E = (1 - x)^2 + x^2 \frac{\rho_l f_g}{\rho_g f_l} \quad (2.50)$$

$$F = x^{0.78} (1 - x)^{0.224} \quad (2.51)$$

$$H = \left(\frac{\rho_l}{\rho_g}\right)^{0.91} \left(\frac{\mu_g}{\mu_l}\right)^{0.19} \left(1 - \frac{\mu_g}{\mu_l}\right)^{0.7} \quad (2.52)$$

$$We_l = \frac{G^2 D_{ab,i}}{\sigma \rho_h} \quad (2.53)$$

Equation 2.53 is the Weber number which is the ratio of inertia to surface tension forces. In Equation 2.53, ρ_h is the homogenous density which depends on the vapor quality calculated by Equation 2.54.

$$\rho_h = \left(\frac{x}{\rho_g} + \frac{1-x}{\rho_l}\right)^{-1} \quad (2.54)$$

2.1.6 Computer Code

A computer code is developed in order to simulate the same DSG solar collector array simulated in the INDITEP project and shown in Figure 1.12. Design point parameters and the parameters of ET-100 collectors used in the model are presented in Table 2.2 and Table 2.3 [21].

Table 2.2 Design Point Parameters [21]

Direct solar irradiance	875 W/m ²
Geographical longitude of the site	W 5° 58'
Geographical latitude of the site	N 37° 24'
Air temperature	20 °C
Incidence angle of solar radiation	13.7°

As shown in Table 2.3, one collector length is 98.5 m and every collector is made of 8 modules having 12.27 m length. In the mathematical model, every module is divided by 10 sub-modules having 1.227 m length. The mathematical code is developed to model a single collector as a sum of 80 sub-modules. It is assumed that every sub-module's absorber temperature is constant throughout the sub-module. One sub-module's outlet conditions are equal to the inlet conditions of the continuing sub-module as shown in the Figure 2.10. Inlet conditions of one array are taken as the same given in [21], which are shown in Table 2.4.

Table 2.3 Parameters of ET-100 Parabolic Trough Collectors [21]

Overall length of a single collector (m)	98.5
Number of parabolic trough modules per collector	8
Gross length of every module (m)	12.27
Parabola width (m)	5.76
Outer diameter of steel absorber (m)	0.07
Inner diameter of steel absorber pipe (m)	0.055
Length of pipe connecting adjacent collectors (m)	5
Number of 90° elbows between adjacent collectors	4
Number of ball joints between adjacent collectors	4
Net collector aperture per collector (m ²)	548.35
Peak optical efficiency	0.765
Cross section of the steel absorber pipes (m ²)	2.40E-01
Innner roughness factor of the steel absorber pipes	4.0E-05
Relative roughness of the steel absorber pipes	7.23E-04

In order to determine water steam properties, an open source code is used called XSteam [34], which is a function that can be called by Matlab and MS Excel by writing required

inputs, to get an output. The code is based on International Association for Properties of Water and Steam Industrial Formulation 1997 (IAPWS IF-97).

For the start of the code in the liquid phase, inlet conditions are defined in Table 2.4. The code starts with an initial absorber temperature (T_{ab}). Absorber temperature is initially estimated as 30°C higher than the inlet temperature. Table 2.4 shows the design inlet conditions for the design.

Table 2.4 Inlet Conditions for Design [21]

Pressure (bars)	80
Temperature (°C)	153
Mass Flow Rate (kg/s)	1.42
Ethalpy (kJ/kg)	650

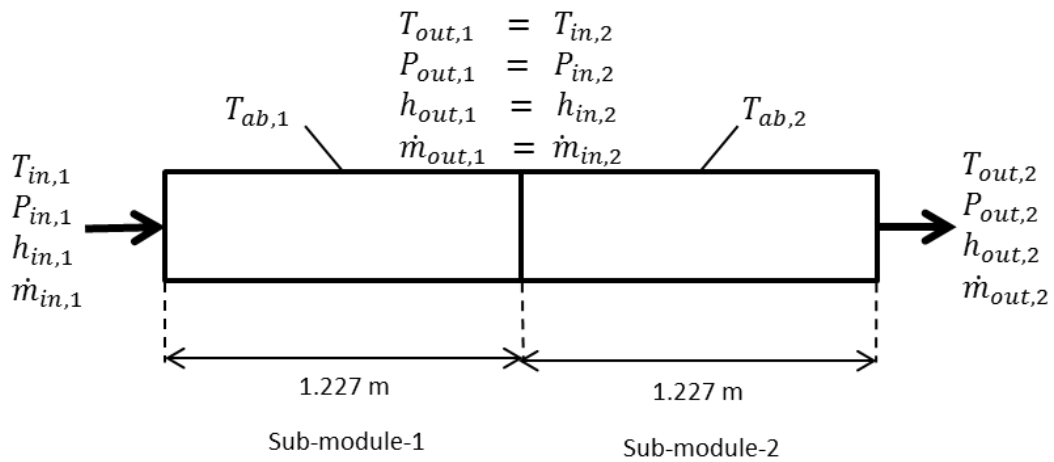


Figure 2.10 Connection Between Sub-modules

Using Equation 2.13) heat losses are calculated and total heat absorbed is calculated. Using the absorber temperature, an initial mean fluid temperature and initial average pressure are defined as,

$$T_{mean,initial} = \frac{T_{in} + T_{ab}}{2} \quad (2.55)$$

$$P_{ave,initial} = P_{in} \quad (2.56)$$

Using the mean temperature, all the fluid properties required for the convection heat transfer coefficient are calculated. Also the properties required for pressure loss calculations described in Section 2.15 are done using the mean temperature.

Using the convection heat transfer coefficient, and thermal conductivity obtained by Equation 2.39, the overall heat transfer coefficient is calculated using Equation 2.38. Using the overall heat transfer coefficient, an outlet temperature is calculated by Equation 2.40.

The outlet pressure is calculated by using the equations explained in Section 2.1.5,

$$P_e = P_{in} - \Delta P \quad (2.57)$$

After the outlet pressure is calculated, the average pressure for the sub-module is calculated as,

$$P_{ave} = \frac{P_{in} + P_e}{2} \quad (2.58)$$

Using the calculated outlet temperature, a new mean temperature is calculated as,

$$T_m = \frac{T_e + T_{in}}{2} \quad (2.59)$$

The new mean temperature calculated by Equation 2.59, is used for calculating the new absorber temperature stated in [22] by using the new mean temperature calculated by Equation 2.60.

$$T_{ab} = T_m + \frac{Q_{net}}{U2\pi rL} \quad (2.60)$$

where U is the overall heat transfer coefficient, r is the inner radius of the absorber tube, and L is the length of the sub-module.

By using the XSteam function, the outlet enthalpy corresponding to the outlet pressure and temperature is calculated.

After calculating the outlet pressure, outlet temperature, new mean temperature and new absorber temperature, the calculations are done again from the beginning for the same sub-module. This time the mean temperature, average pressure and absorber temperature used are from the calculated values of the previous iteration.

Five iterations are required for all the outlet conditions to converge for a sub-module, with the changes between the 4th and 5th iterations being less than 1%.

The calculations stated above are done for all sub-modules and 80 sub-module minor pressure drops are also calculated. At the end of every sub-module, the program checks if the exit temperature reached the saturation temperature of water at that pressure.

If the exit temperature reaches the saturation temperature of water at that pressure, the two phase part of the code is activated. For the two phase part of the code, every step is the same with the one phase part of the code explained above except the outlet enthalpy. Since in the two phase region the inlet and the exit temperatures are equal, the outlet enthalpy is calculated as,

$$h_e = h_{in} + \frac{Q_{net}}{\dot{m}} \quad (2.61)$$

The pressure drop calculation also has one code for one phase and another for two phase flow. At the end of every sub-module, the code checks if the quality of the flow is bigger than 0. If the quality is bigger than 0, the two phase pressure drop calculation is activated.

Figure 2.11 presents a flowchart for the computer code for the Matlab code developed.

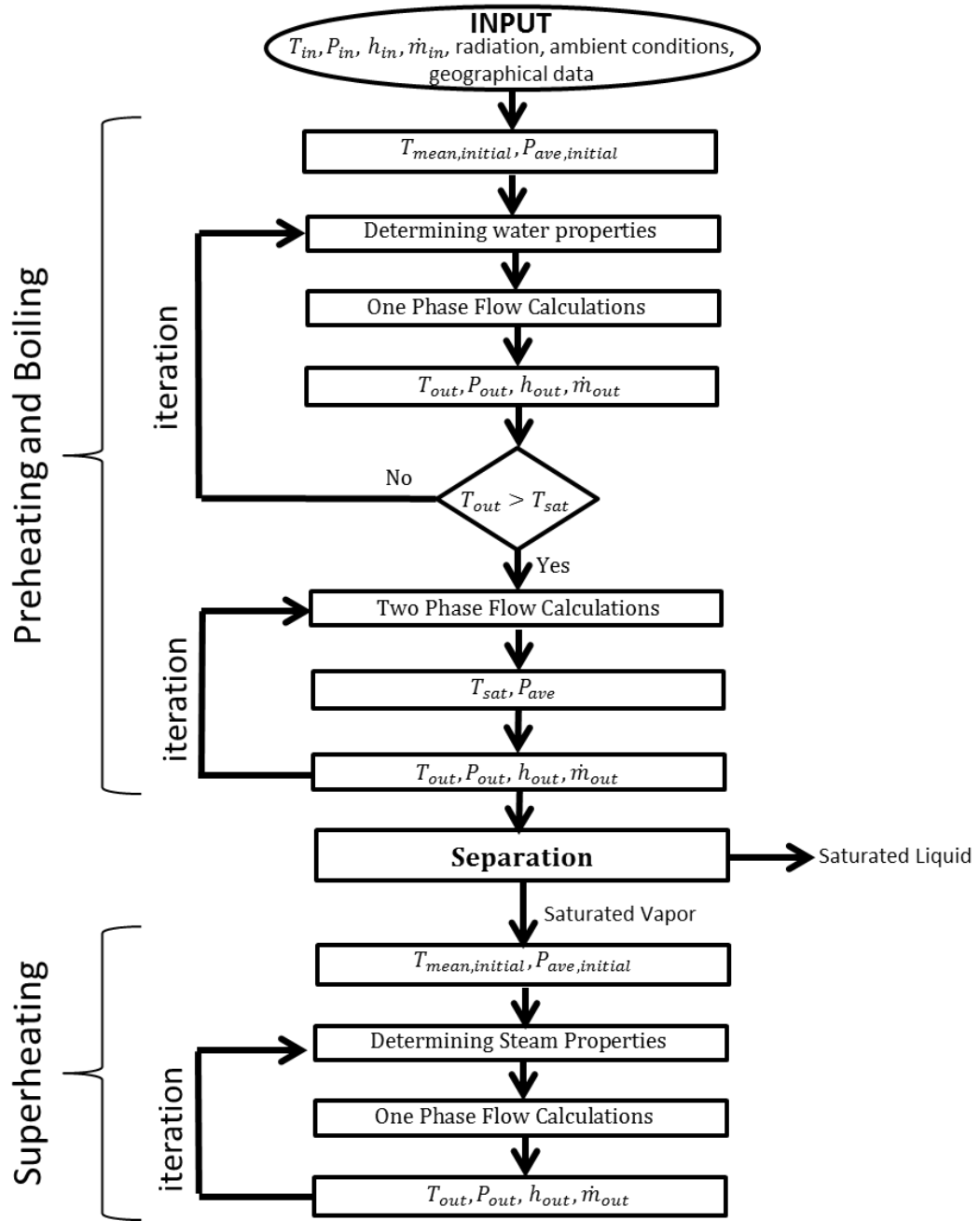


Figure 2.11 Flow Chart of the Matlab Code

The mass specific enthalpy after injection and before the last superheating collector is calculated as,

$$h_{\text{total}} = \frac{(m_{\text{inj}}h_{\text{inj}}) + (m_{\text{sh},1}h_{\text{sh},1})}{m_{\text{inj}} + m_{\text{sh},1}} \quad (2.62)$$

In Equation 2.62, the subscript inj is for injection and sh,1 is for the outlet of the first superheating collector.

2.1.7 Benchmarking

The computer code is run for design point parameters mentioned in Table 2.2, Table 2.3 and Table 2.4. The results are compared with the published data of [21] for the collector system presented in Figure 1.12. In [21], the inlet conditions for wind speed, ambient temperature and dew point temperature are not given. Table 2.5, Table 2.6 and Table 2.7 presents results and benchmarking.

Table 2.5 Benchmarking Outlet of Preheat-Boiling Section

	Simulation Result	INDITEP Result	Difference
\dot{m} (kg/s)	1,42	1,42	0,00%
P (bars)	74,80	75	0,27%
T (°C)	290,4	290	0,12%
h (kJ/kg)	2472	2434	1,57%

Table 2.6 Benchmarking Outlet of First Superheating Section

	Simulation Result	INDITEP Result	Difference
\dot{m} (kg/s)	1,13	1,10	2,73%
P (bars)	71,33	71,70	0,52%
T (°C)	355,8	362	1,72%
h (kJ/kg)	3031	3046	0,50%

Table 2.7 Benchmarking Outlet of Second Superheating Section

	Simulation Result	INDITEP Result	Difference
\dot{m} (kg/s)	1,17	1,17	0,00%
P (bars)	69,74	69,90	0,24%
T (°C)	419,2	411	1,99%
h (kJ/kg)	3210	3186	0,76%

As shown in Tables 2.5, 2.6 and 2.7, good agreement is found between the published data and the simulation results.

Since the outlet enthalpy at the outlet of the preheating and boiling section is 1% higher than the published data, the amount of steam passed to the superheating collector is 0.03 kg/s higher. This behavior makes the first superheating section outlet temperature and enthalpy lower than the published data.

In order to have the same mass flow rate at the outlet of the second superheating section, the same Injection conditions are used as stated in Figure 2.13, but with a difference in mass flow rate. Mass flow rate of the injection as taken as 0.04 kg/s.

CHAPTER 3

DSG SIMULATIONS

3.1 Parametric Studies

The model presented and benchmarked against the published data in Chapter 2 is used for parametric studies in this chapter.

In order to give information about the performance of the solar array simulated for different inlet conditions, simulations are run for different inlet temperatures, for variable DNI's and working pressures. For the simulations presented in this chapter, all other conditions stated in Chapter 2 are conserved.

It is important to state that the last collector, called the second superheating collector, is not used in parametric studies. The reason is to neglect water injection to the second superheating collector in order to make a correct comparison.

For the parametric studies, collector inlet temperatures from 20°C to 200°C are assumed with 20°C increments. Simulations are performed for these inlet temperatures for working pressures of 60 bars, 80 bars, 100 bars and 120 bars. All the other parameters are fixed and the same as in Chapter 2. Another parametric study is done for varying DNI from 400W/m² to 1000W/m² with 200W/m² increments.

In order to state the amount of steam power produced, the term thermal power is used in this chapter.

$$\text{Thermal Power} = h_{sh} \dot{m}_{sh} \quad (3.1)$$

Another term used in this chapter is efficiency. The efficiency of the entire system is calculated as,

$$\mu_{sys} = \frac{(\dot{m}_{cond} h_{cond}) + (\dot{m}_{sh} h_{sh}) - (\dot{m}_{in} h_{in})}{DNI \cos \theta (A)} \quad (3.2)$$

In Equation 3.2, A is the sum of aperture areas of all 9 collectors. In some cases stated in this chapter, solar resources are not enough to produce steam in preheating and boiling section. For such cases, superheating collector is not used and the total aperture area is taken as the sum of 8 collectors used for preheating, not boiling.

Table 3.1 and Figure 3.1 present the results for 60 bars inlet pressure.

Table 3.1 Results for Inlet pressure of 60 bars

Inlet Conditions		Condensed Liquid		Preheat and Boiling				Superheating			
T (°C)	h (kJ/kg)	h (kJ/kg)	\dot{m} (kg/s)	T (°C)	h (kJ/kg)	x (-)	p (bars)	T (°C)	h (kJ/kg)	p (bars)	\dot{m} (kg/s)
20	89,55	1197	0,90	272,5	1782	0,37	57,21	459,32	3333	54,80	0,52
40	172,84	1194	0,80	271,8	1888	0,44	56,56	425,89	3254	53,63	0,62
60	256,17	1188	0,71	270,6	1994	0,50	55,56	401,88	3198	52,01	0,71
80	339,69	1181	0,61	269,3	2100	0,57	54,45	384,00	3157	50,19	0,81
100	423,53	1174	0,51	268,0	2206	0,64	53,34	370,20	3126	48,28	0,91
120	507,87	1163	0,42	265,7	2313	0,71	51,44	358,90	3104	45,32	1,00
140	592,87	1152	0,32	263,6	2421	0,77	49,71	349,70	3087	42,42	1,10
160	678,73	1136	0,23	260,3	2530	0,84	47,16	341,62	3077	38,25	1,19
180	765,73	1118	0,13	256,8	2640	0,91	44,51	334,57	3070	33,66	1,29
200	854,22	1094	0,04	251,7	2753	0,97	40,92	327,71	3069	27,47	1,38

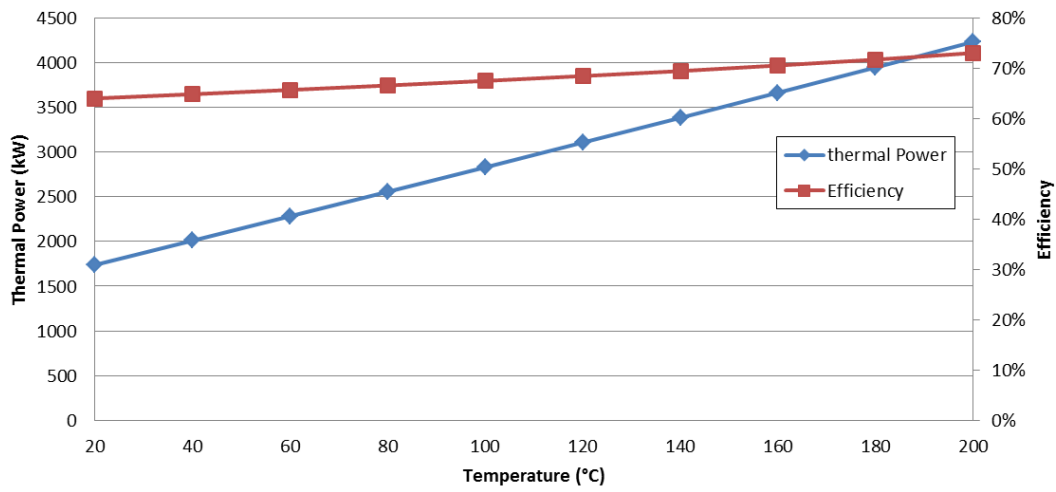


Figure 3.1 Thermal Power Produced and Efficiency for Variable Inlet Temperatures for 60 Bars Inlet Pressure

Table 3.2 and Figure 3.2 present the results for 80 bars inlet pressure.

Table 3.2 Results for Inlet pressure of 80 bars

Inlet Conditions		Condensed Liquid		Preheat and Boiling				Superheating			
T (°C)	h (kJ/kg)	h (kJ/kg)	\dot{m} (kg/s)	T (°C)	h (kJ/kg)	x (-)	p (bars)	T (°C)	h (kJ/kg)	p (bars)	\dot{m} (kg/s)
20	91,42	1309	0,98	293,6	1756	0,31	78,42	499,26	3401	77,35	0,44
40	174,61	1307	0,88	293,3	1861	0,38	78,09	451,55	3282	76,75	0,54
60	257,85	1306	0,78	293,1	1967	0,45	77,78	420,28	3202	76,14	0,64
80	341,28	1304	0,67	292,7	2073	0,53	77,33	398,54	3145	75,38	0,75
100	425,04	1301	0,57	292,2	2179	0,60	76,77	382,69	3102	74,46	0,85
120	509,28	1298	0,46	291,7	2286	0,67	76,23	370,68	3070	73,54	0,96
140	594,18	1294	0,36	290,9	2394	0,75	75,36	361,12	3045	72,22	1,06
160	679,92	1290	0,25	290,1	2503	0,82	74,56	353,46	3025	70,97	1,17
180	766,77	1284	0,15	289,1	2613	0,90	73,46	346,90	3009	69,39	1,27
200	855,06	1279	0,04	288,1	2726	0,97	72,35	341,19	2996	67,89	1,38

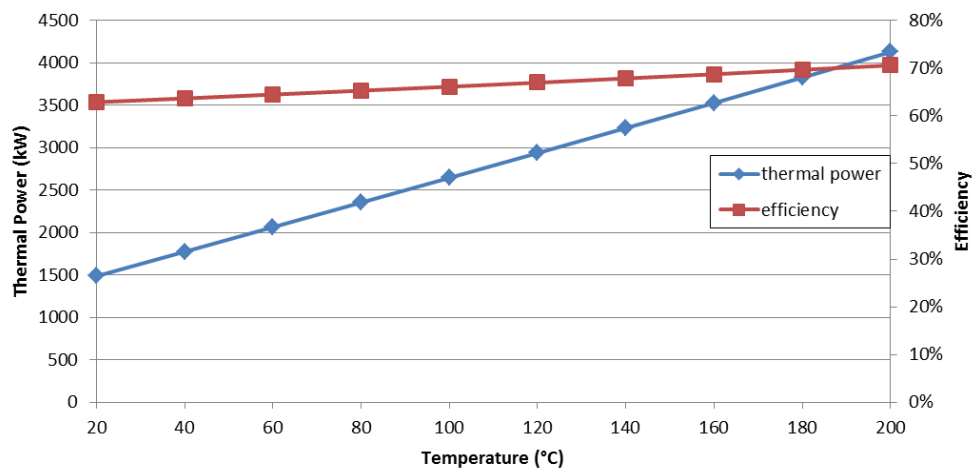


Figure 3.2 Thermal Power Produced and Efficiency for Variable Inlet Temperatures for 80 Bars Inlet Pressure

Table 3.3 and Figure 3.3 present the results for 100 bars inlet pressure.

Table 3.3 Results for Inlet pressure of 100 bars

T (°C)	h (kJ/kg)	h (kJ/kg)	\dot{m} (kg/s)	T (°C)	h (kJ/kg)	x (-)	p (bars)	T (°C)	h (kJ/kg)	p (bars)	\dot{m} (kg/s)
20	93,29	1401	1,06	310,0	1734	0,25	98,62	551,85	3508	98,07	0,36
40	176,37	1401	0,95	310,0	1839	0,33	98,60	479,46	3324	97,89	0,47
60	259,53	1400	0,84	309,9	1944	0,41	98,44	437,15	3211	97,55	0,58
80	342,87	1400	0,73	309,7	2050	0,49	98,28	410,35	3135	97,19	0,69
100	426,55	1399	0,61	309,6	2156	0,57	98,05	392,14	3080	96,74	0,81
120	510,70	1397	0,50	309,3	2263	0,65	97,74	379,09	3040	96,19	0,92
140	595,49	1396	0,38	309,1	2370	0,73	97,45	369,35	3009	95,64	1,04
160	681,11	1394	0,27	308,7	2479	0,81	96,95	361,71	2984	94,86	1,15
180	767,81	1392	0,15	308,4	2589	0,89	96,51	355,62	2965	94,14	1,27
200	855,92	1389	0,03	307,9	2701	0,98	95,90	350,47	2948	93,31	1,39

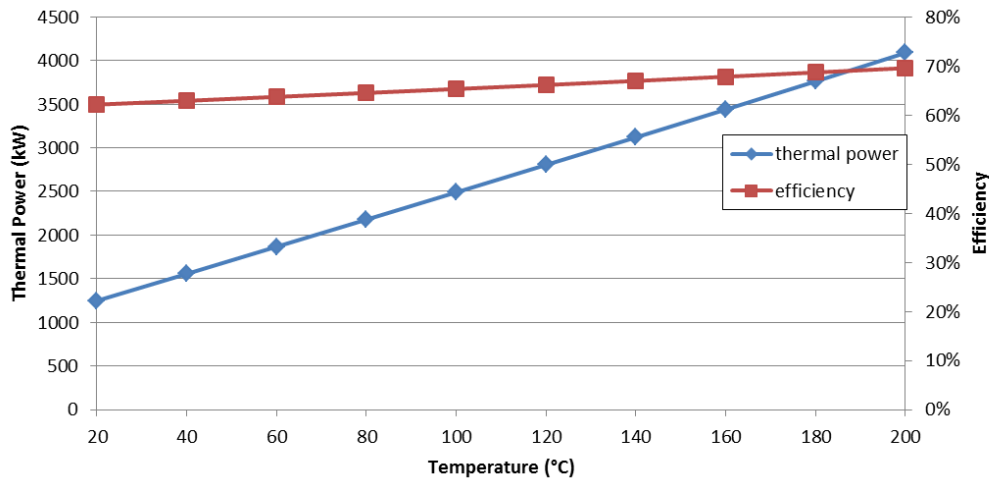


Figure 3.3 Thermal Power Produced and Efficiency for Variable Inlet Temperatures for 100 Bars Inlet Pressure

Table 3.4 and Figure 3.4 present the results for 120 bars inlet pressure.

Table 3.4 Results for Inlet pressure of 120 bars

Inlet Conditions		Condensed Liquid		Preheat and Boiling				Superheating			
T (°C)	h (kJ/kg)	h (kJ/kg)	\dot{m} (kg/s)	T (°C)	h (kJ/kg)	x (-)	ρ (bars)	T (°C)	h (kJ/kg)	ρ (bars)	\dot{m} (kg/s)
20	95,15	1485	1,15	323,8	1713	0,19	118,66	642,36	3716	118,37	0,27
40	178,14	1485	1,03	323,8	1818	0,28	118,64	516,28	3396	118,25	0,39
60	261,20	1485	0,90	323,8	1924	0,36	118,67	455,13	3228	118,15	0,52
80	344,46	1485	0,78	323,8	2029	0,45	118,59	420,96	3125	117,93	0,64
100	428,06	1485	0,65	323,7	2135	0,54	118,53	399,63	3056	117,71	0,77
120	512,12	1484	0,53	323,7	2242	0,63	118,40	385,38	3006	117,41	0,89
140	596,81	1483	0,40	323,5	2349	0,72	118,23	375,26	2969	117,06	1,02
160	682,31	1483	0,27	323,4	2457	0,81	118,07	367,82	2941	116,70	1,15
180	768,86	1482	0,14	323,3	2568	0,90	117,77	362,01	2918	116,19	1,28
200	856,79	1481	0,01	323,1	2679	0,99	117,52	357,37	2899	115,81	1,41

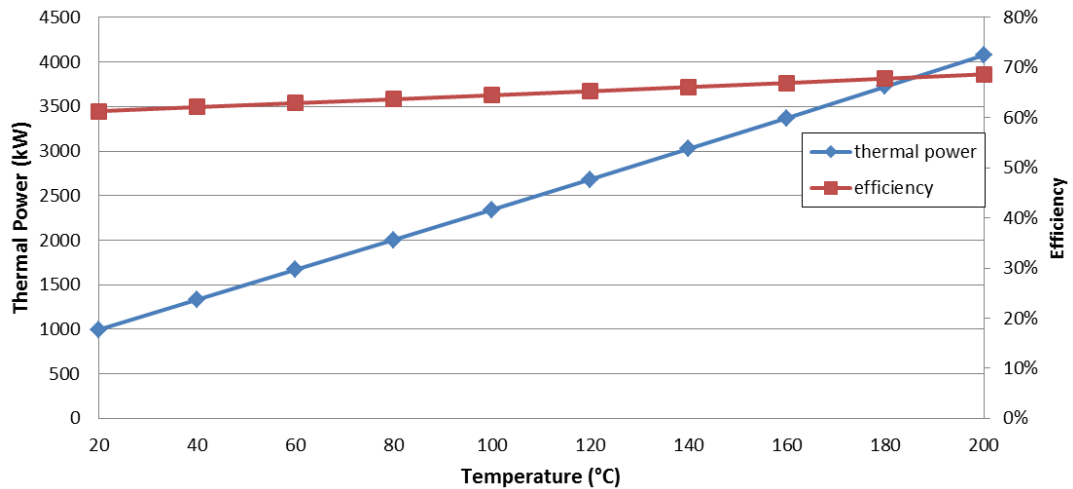


Figure 3.4 Thermal Power Produced and Efficiency for Variable Inlet Temperatures for 120 Bars Inlet Pressure

As the working pressure increases the total pressure drop is decreasing. For 60 bars, the saturation temperature is lower than the other 3 cases because of the lower pressure. This makes the thermal heat losses lower, since thermal losses increase with absorber temperature and the 2-phase portion of the collector is operating at a lower temperature. On the other hand, as the quality of the flow leaving the preheating and boiling collectors increases, the pressure drop in the two-phase region of the system increases. As a result of the high pressure drop, the required pump power to drive the system increases. Therefore there is a trade-off between maximizing the efficiency of the system and the end power consumption of the pump used in such a system.

Another parametric study was performed for variable DNI's. In this case, the pressure is kept constant at 80 bars. Table 3.5 and Figure 3.5 present results for DNI=400 W/m².

Table 3.5 Results for DNI=400 W/m²

Inlet Conditions		Condensed Liquid		Preheat and Boiling				Superheating			
<i>T</i> (°C)	<i>h</i> (kJ/kg)	<i>h</i> (kJ/kg)	<i>m</i> (kg/s)	<i>T</i> (°C)	<i>h</i> (kJ/kg)	<i>x</i> (-)	<i>p</i> (bars)	<i>T</i> (°C)	<i>h</i> (kJ/kg)	<i>p</i> (bars)	<i>m</i> (kg/s)
20	91,42	809	1,42	189,6	809	0,00	78,52				
40	174,61	892	1,42	208,3	892	0,00	78,62				
60	257,85	975	1,42	226,5	975	0,00	78,70				
80	341,28	1058	1,42	244,3	1058	0,00	78,76				
100	425,04	1142	1,42	261,5	1142	0,00	78,82				
120	509,28	1226	1,42	278,1	1226	0,00	78,88				
140	594,18	1310	1,42	293,8	1310	0,00	78,93				
160	679,92	1312	1,32	294,2	1418	0,07	79,05	724,07	3941	78,70	0,10
180	766,77	1311	1,21	294,0	1528	0,15	78,83	481,29	3355	78,27	0,21
200	855,06	1309	1,10	293,6	1640	0,23	78,40	404,31	3156	77,61	0,32

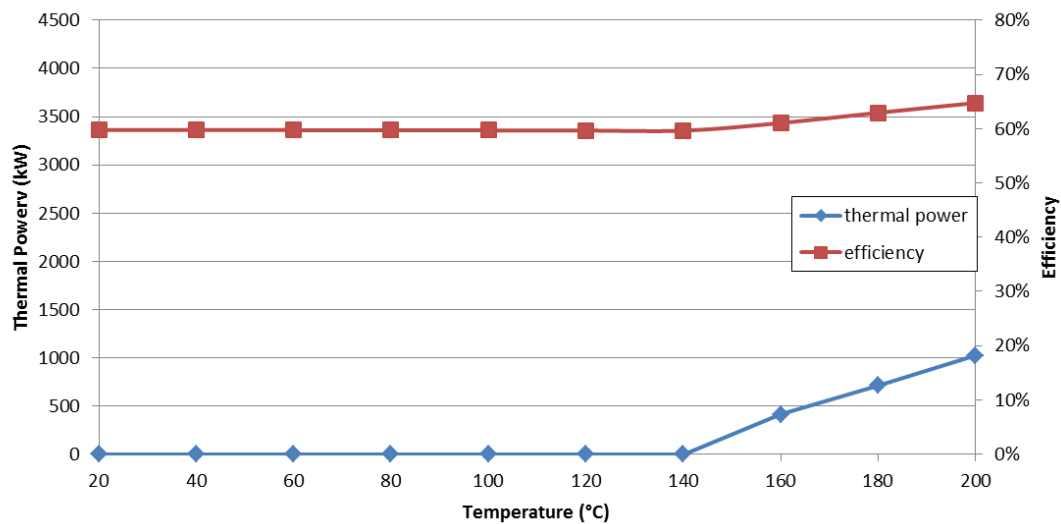


Figure 3.5 Thermal Power Produced and Efficiency for Variable Inlet Temperatures for DNI=400 W/m²

As shown in Table 3.5, for DNI = 400 W/m², no steam is generated until the inlet temperature reaches 160°C. The radiation is not sufficient to create steam in the preheating and boiling section which consists of 8 collectors. If such a system were to be used with temperatures lower than 160°C, additional collectors must be used to generate steam.

Table 3.6 and Figure 3.6 present the results for DNI = 600 W/m².

Table 3.6 Results for DNI=600 W/m²

Inlet Conditions		Condensed Liquid		Preheat and Boiling				Superheating			
T (°C)	h (kJ/kg)	h (kJ/kg)	\dot{m} (kg/s)	T (°C)	h (kJ/kg)	x (-)	ρ (bars)	T (°C)	h (kJ/kg)	ρ (bars)	\dot{m} (kg/s)
20	91,42	1168	1,42	266,7	1168	0,00	78,67				
40	174,61	1251	1,42	282,8	1251	0,00	78,75				
60	257,85	1311	1,42	294,0	1340	0,02	78,83				
80	341,28	1311	1,29	294,1	1446	0,09	78,93	817,19	4167	78,52	0,13
100	425,04	1311	1,18	293,9	1551	0,17	78,75	567,20	3565	78,14	0,24
120	509,28	1309	1,08	293,7	1658	0,24	78,53	467,76	3322	77,69	0,34
140	594,18	1308	0,97	293,4	1766	0,31	78,18	417,42	3193	77,09	0,45
160	679,92	1305	0,87	292,9	1875	0,39	77,64	387,84	3113	76,26	0,55
180	766,77	1302	0,76	292,4	1985	0,47	77,10	368,84	3060	75,41	0,66
200	855,06	1298	0,65	291,6	2097	0,54	76,21	355,42	3022	74,15	0,77

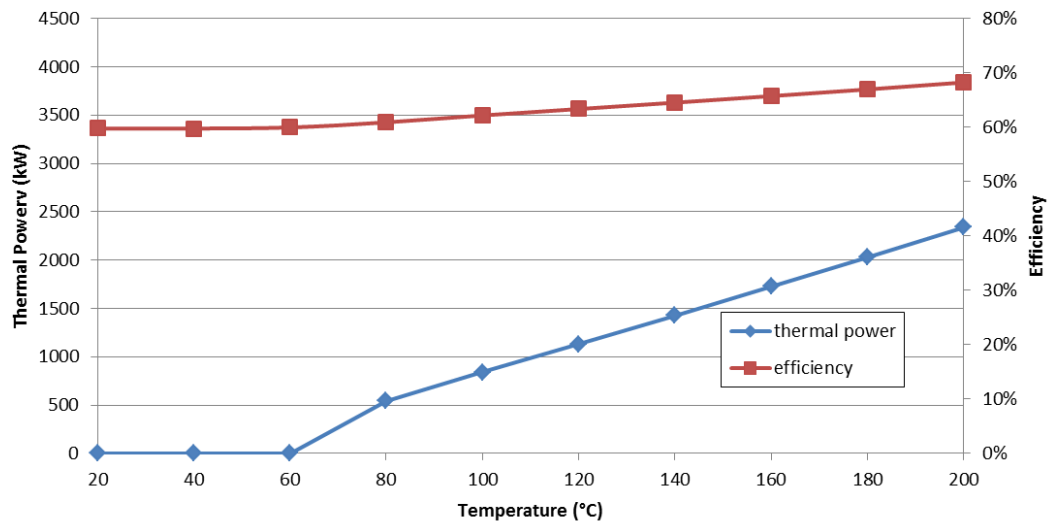


Figure 3.6 Thermal Power Produced and Efficiency for Variable Inlet Temperatures for DNI=600 W/m²

Table 3.7 and Figure 3.7 present the results for DNI=800 W/m².

Table 3.7 Results for DNI=800 W/m²

Inlet Conditions		Condensed Liquid		Preheat and Boiling				Superheating			
T (°C)	h (kJ/kg)	h (kJ/kg)	\dot{m} (kg/s)	T (°C)	h (kJ/kg)	x (-)	p (bars)	T (°C)	h (kJ/kg)	p (bars)	\dot{m} (kg/s)
20	91,42	1310	1,15	293,8	1585	0,19	78,65	623,91	3701	77,95	0,27
40	174,61	1309	1,05	293,7	1690	0,26	78,53	517,56	3445	77,61	0,37
60	257,85	1308	0,94	293,5	1796	0,34	78,25	458,69	3300	77,08	0,48
80	341,28	1306	0,84	293,2	1902	0,41	77,92	422,40	3207	76,47	0,58
100	425,04	1304	0,73	292,8	2008	0,48	77,48	398,18	3143	75,72	0,69
120	509,28	1302	0,63	292,3	2115	0,56	76,92	381,02	3097	74,82	0,79
140	594,18	1299	0,52	291,8	2223	0,63	76,38	368,27	3062	73,91	0,90
160	679,92	1294	0,42	291,0	2331	0,70	75,46	358,33	3035	72,56	1,00
180	766,77	1290	0,31	290,2	2442	0,78	74,65	350,42	3015	71,30	1,11
200	855,06	1284	0,21	289,1	2554	0,86	73,44	343,76	2999	69,58	1,21

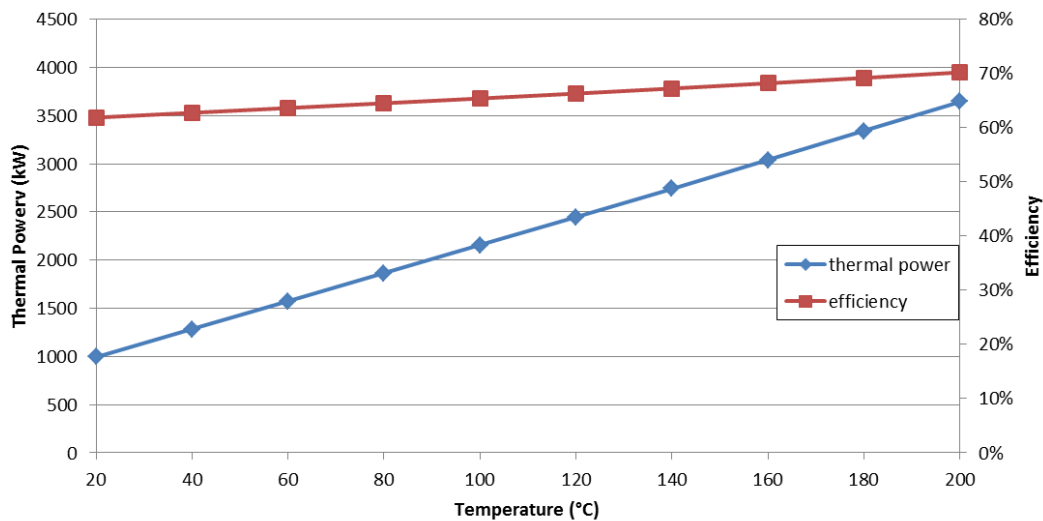


Figure 3.7 Thermal Power Produced and Efficiency for Variable Inlet Temperatures for DNI=800 W/m²

Table 3.8 and Figure 3.8 present the results for DNI=1000 W/m²

Table 3.8 Results for DNI=1000 W/m²

Inlet Conditions		Condensed Liquid		Preheat and Boiling				Superheating			
T (°C)	h (kJ/kg)	h (kJ/kg)	\dot{m} (kg/s)	T (°C)	h (kJ/kg)	x (-)	p (bars)	T (°C)	h (kJ/kg)	p (bars)	\dot{m} (kg/s)
20	91,42	1305	0,70	292,9	2042	0,51	77,63	424,97	3215	75,77	0,72
40	174,61	1304	0,60	292,7	2147	0,58	77,32	404,67	3162	75,13	0,82
60	257,85	1301	0,50	292,1	2253	0,65	76,70	389,26	3121	74,13	0,92
80	341,28	1298	0,39	291,6	2358	0,72	76,16	377,44	3090	73,20	1,03
100	425,04	1294	0,29	291,0	2465	0,80	75,47	367,91	3065	72,08	1,13
120	509,28	1290	0,19	290,2	2572	0,87	74,65	360,07	3045	70,80	1,23
140	594,18	1286	0,08	289,5	2679	0,94	73,84	353,45	3029	69,59	1,34

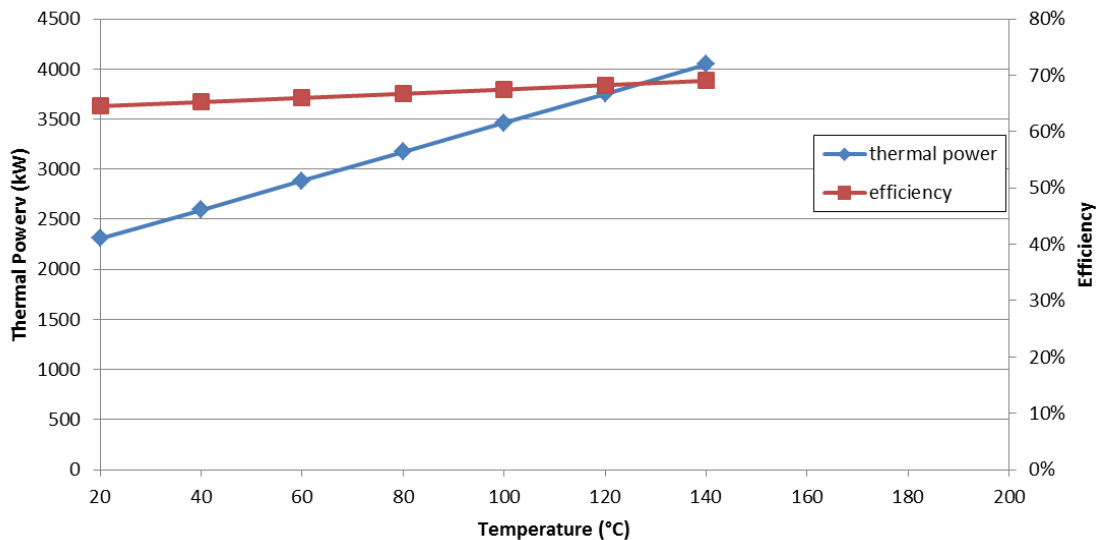


Figure 3.8 Thermal Power Produced and Efficiency for Variable Inlet Temperatures for DNI=1000 W/m²

For DNI=1000 W/m² and inlet temperature of 140 °C, a vapor quality of 0.94 is generated by the preheating and boiling section of the system. Further increasing the inlet temperature beyond 140°C makes the quality equal to 1 before the outlet of preheat and boiling section. In this case, the last collector may be defocused in order to have condensed liquid at the separator.

For variable DNI parametric study, for lower DNI's for all inlet temperatures or higher DNI's with low inlet temperatures, very low quality steam is produced ranging from 0.07 to 0.19. In such situations, mass flow rate to the superheating collector becomes very low. This low mass flow rate causes the steam temperature to increase to 818 °C, which can damage the absorbers. In the control strategy of such a facility, the superheating collectors must be defocused. This should be arranged according to the inlet temperature and solar resources

available at that instance. Another control strategy can be adapted to adjust the inlet temperature so that the exit vapor quality can exceed some critical level.

For higher DNI's, the inlet temperature should be kept below certain levels. In the DSG simulation, the maximum inlet temperature level is 160°C for 1000 W/m². For the higher DNI's explored in this work, the liquid flow rate from the separator decreases as the inlet temperature increases.

CHAPTER 4

CSP MODEL AND SIMULATIONS

In this chapter, a CSP solar array that is used to produce superheating steam for a power plant simulation is proposed using the DSG model presented in Chapter 3 and TRNSYS 17 software [35].

The DSG model presented in Chapter 3 is separated into 3 different models: 1) preheating and boiling; 2) the first superheating section; and 3) the second superheating section of the system.

4.1 Simulation of a Solar Array

In this simulation, a CSP solar array using DSG is modeled using the DSG model presented in Chapter 3. In the model, as presented in Chapter 3, 8 ET-100 collectors are used for preheating and boiling, and 2 collectors are used for superheating. Figure 4.1 presents the schematic representation of the system.

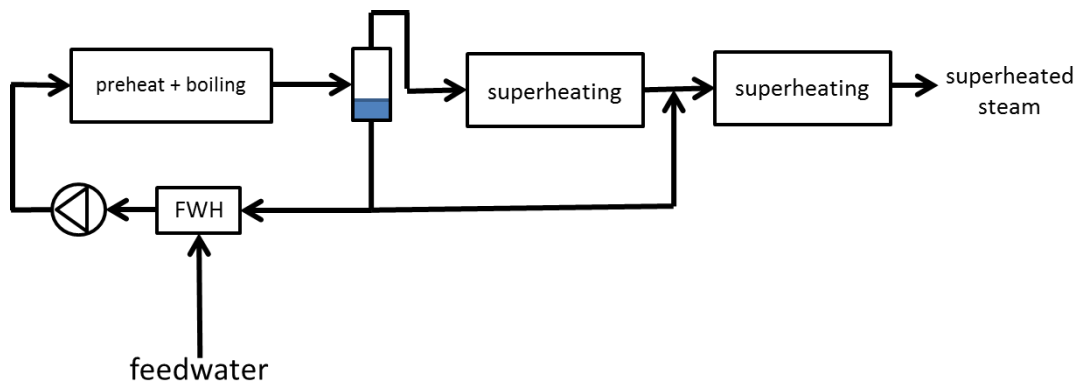


Figure 4.1 Schematic Representation of DSG Solar Array Model

In this section, a model for a steam generating solar array is presented. It is assumed that a CSP field using DSG technology is used for generating steam rather than generating electricity.

In this model, after the preheating and boiling section, there is a steam separator that separates vapor and liquid water. The vapor phase of the flow leaving the separator passes through the first superheating collector. 20% of the liquid phase of the flow leaving the steam separator is mixed with the outlet of the first superheating collector. This is done to control the outlet steam temperature manually and in the model as a first approximation the portion directed for mixing is fixed. The other 80% of the liquid water leaving the separator is directed to the feedwater heater.

In the feedwater heater, the liquid water from the separator is mixed with feedwater. The feedwater temperature is fixed at 25°C and 20 bars. The flow rate of the feedwater is arranged to have an outlet flow rate equal to 1.42 kg/s so that the same amount of steam produced is fed to the system.

$$\dot{m}_{fw} = 1.42 - \dot{m}_{sh} \quad (4.1)$$

Here the subscripts fw and sh represent the feedwater and superheated steam respectively.

After the feedwater heater, the flow is pressurized to 80 bars. In Figure 4.2 the TRNSYS model of the solar collector array is presented.

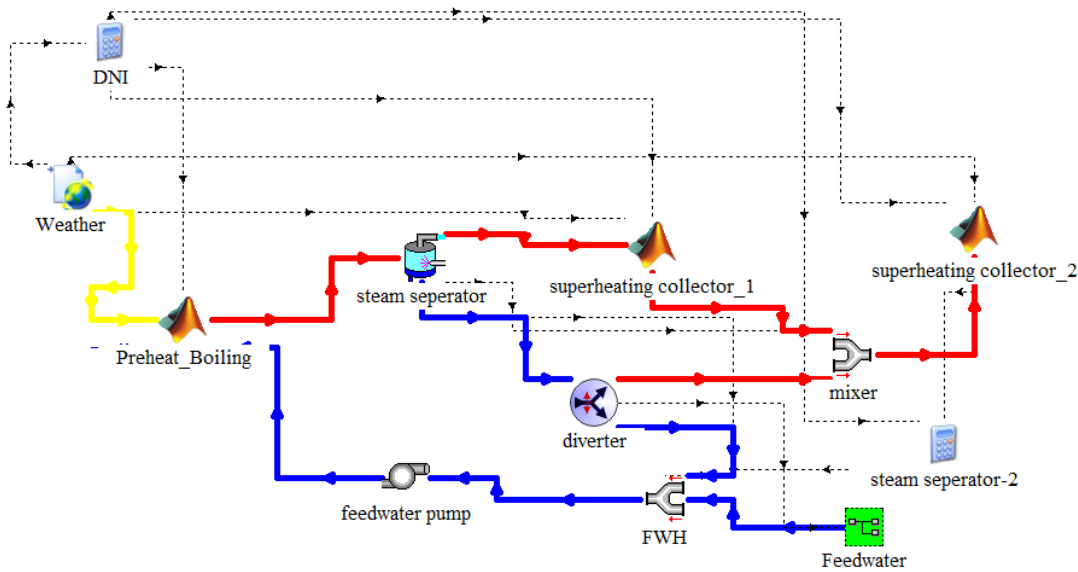


Figure 4.2 TRNSYS Model of Solar Array

TRNSYS Type 15 is used for the weather data. In this simulation, Almeria airport TMY2 data is used from the Meteornorm data provided with the TRNSYS software. The DSG Model is called by TRNSYS via Type 155 Calling Matlab. Table 4.1 shows the geographical information for Almeria airport.

Table 4.1 Geographical Information of Almeria Airport

Time Zone	1
Latitude	N 36° 51'
Longitude	W 2° 23'

Table 4.2 shows the Inputs to the Type 155 Calling Matlab Inputs that are connected to Type 15 Weather Data.

Table 4.2 Input to Type 155 from Weather Data

Input	Symbol
Number of day	n
Latitude	φ
Longitude	ϕ
Hour of day	i
Effective sky temperature	T_{sky}
wind speed	v
Ambient Temperature	T_{amb}

Table 4.3 shows the component connections for the TRNSYS model of the solar collector array other than the connection between Type 155 and Type 15.

Table 4.3 Component Connections of the Solar Collector Array Model

#	Model Component	Trnsys Type	Input Connections			
			T	P	m	h
1	Preheat and Boiling	155	$T_{1,i} = T_{2,e}$	$P_{1,i} = P_{2,e}$	$m_{1,i} = m_{2,e}$	$h_{1,i} = h_{2,e}$
2	Feedwater Pump	15	$T_{2,i} = T_{9,e}$	$P_{2,i} = P_{9,e}$	$m_{2,i} = m_{9,e}$	$h_{2,i} = h_{9,e}$
3	Steam Separator	611	$T_{3,i} = T_{1,e}$	$P_{3,i} = P_{1,e}$	$m_{3,i} = m_{1,e}$	$h_{3,i} = h_{1,e}$
4	Diverter	11	$T_{4,i} = T_{3,el}$	$P_{4,i} = P_{3,el}$	$m_{4,i} = m_{3,el}$	$h_{4,i} = h_{3,el}$
5	Superheating Collector 1	155	$T_{5,i} = T_{3,ev}$	$P_{5,i} = P_{3,ev}$	$m_{5,i} = m_{3,ev}$	$h_{5,i} = h_{3,ev}$
6	Mixer	595	$T_{6,i1} = T_{4,e1}$	$P_{6,i1} = P_{4,e1}$	$m_{6,i1} = m_{5,e}$	$h_{6,i1} = h_{5,e}$
			$T_{6,i2} = T_{5,e}$	$P_{6,i2} = P_{5,e}$	$m_{6,i2} = m_{4,e1}$	$h_{6,i2} = h_{4,e1}$
7	Superheating Collector 2	155	$T_{7,i} = T_{6,e}$	$P_{7,i} = P_{6,e}$	$m_{7,i} = m_{6,e}$	$h_{7,i} = h_{6,e}$
8	Feedwater		$T_{8,e} = 25^\circ C$	$P_{8,e} = 20 \text{ bars}$	$m_{8,e} = 1.42 - m_{7,e}$	
9	Feedwater Heater	595	$T_{9,i1} = T_{4,e2}$	$P_{9,i1} = P_{4,e2}$	$m_{9,i1} = m_{4,e2}$	$h_{9,i1} = h_{4,e2}$
			$T_{9,i2} = T_{8,e}$	$P_{9,i2} = P_{8,e}$	$m_{9,i2} = m_{8,e}$	$h_{9,i2} = h_{8,e}$

Subscripts: i= inlet, e=outlet, l=liquid, v=vapor, e1= first outlet

In this model, the pump is working even after sunset, so that water is continuously circulating through the preheater and boiler, separator and diverter. Since the diverter is modeled to direct 20% of liquid to the inlet of the second superheater, there is a need of a dummy separator which is modeled when DNI = 0 and results in all the water outlet of the second superheater being directed to the feedwater heater.

The TRNSYS model of the solar array is run for a summer day with good solar resources (26 June) using Almeria Airport TMY2 data. The results are presented in Figure 4.3.

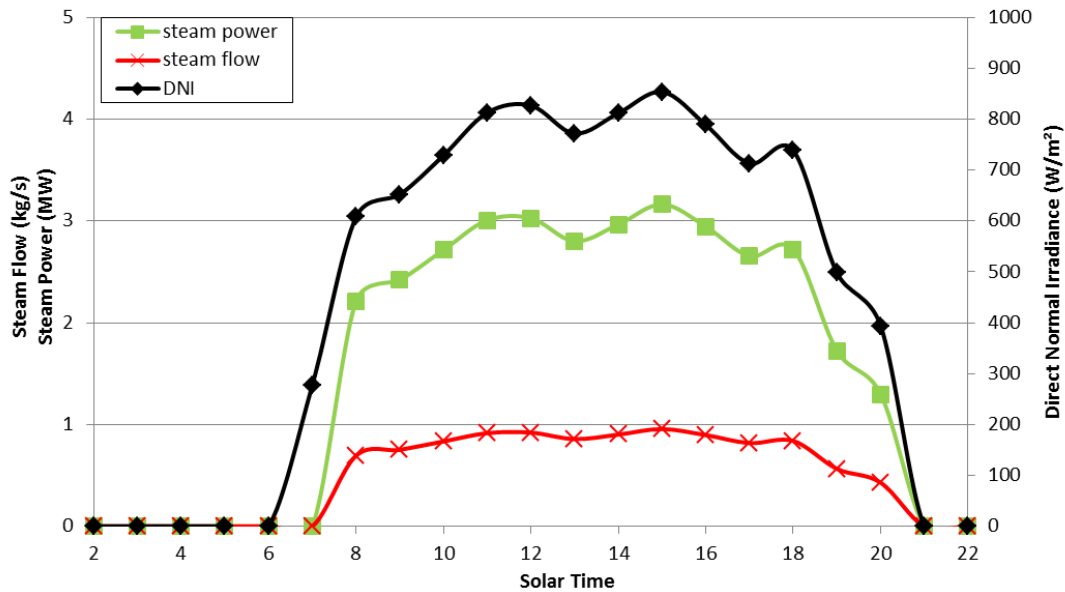


Figure 4.3 Simulation Results for 26 June

Figure 4.3 shows good agreement between the DNI curve, steam flow and steam power curves. The figure shows that on a good summer day with Almeria’s weather conditions, around 3 MW of steam power is produced with steam flow near to 1 kg/s. At 7 am, although DNI exists, no steam is produced. This is because at that time DNI is not sufficient to produce steam as described in Chapter 3.

4.2 Simulation of a CSP Power Plant

In this section, a CSP solar thermal power plant model using DSG technology is presented. In the model, the solar array presented in Section 4.2 is used but the results are calculated for 7 parallel loops as in the reference published work [21].

In the model, additional components are added to the solar array as presented in Section 4.1. Specifically, a three stage steam turbine, condenser, a second diverter and feedwater tank are added. The schematic of the power plant model is shown in Figure 4.4.

The same power block configuration described in [21] is used in the model. The power block model originally consisted of two stages of turbine. The high pressure turbine operates between 65 bars and 5.6 bars. The low pressure turbine operates between 5.6 bars and 0.1 bars. After the high pressure turbine some portion of the steam is directed to the feedwater heater presented in Figure 4.4, after reducing its pressure.

In the TRNSYS model, the low pressure turbine is divided into 2 stages. The first low pressure turbine operates between 5.6 bars and 4 bars. The other low pressure turbine

operates between 4 bars and 0.1 bars. All three turbines have a 72% isentropic efficiency, which is assumed as constant for all flow rates.

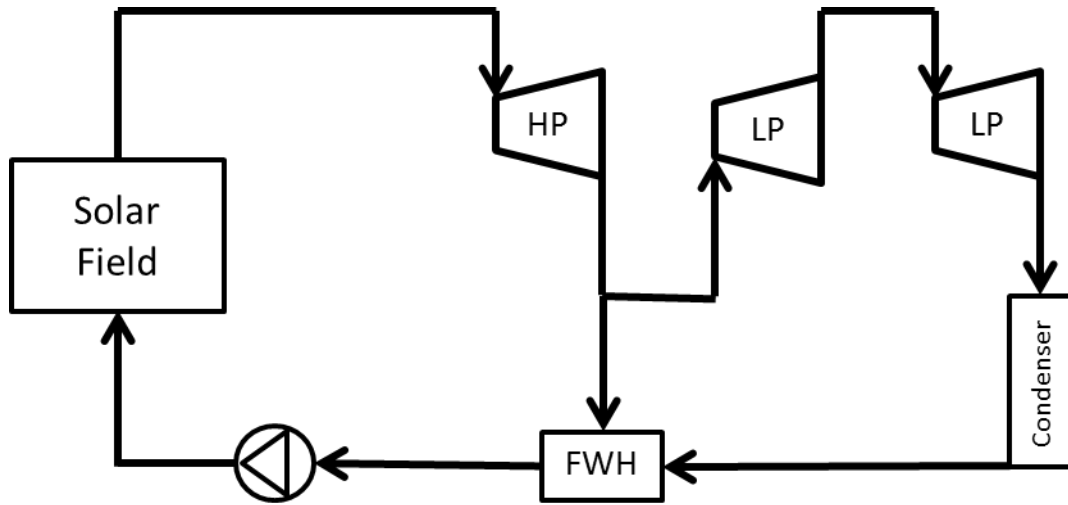


Figure 4.4 Schematic of CSP Solar Power Plant Model

In the TRNSYS model presented here, 10% of the steam flow leaving the HP turbine is directed to the feedwater heater. The feedwater pump used in the model has 90% efficiency.

In this work, when the condenser outlet was attached to the feedwater heater inlet to complete the cycle convergence problems occurred. In order to have the model work, two different assumptions were made and two different cases are simulated in this work. The first case is setting the outlet of the pump to a constant 153 °C temperature with 80 bars pressure, which is the design condition of one loop collector array as presented in Chapter 3. The second case is setting the Feedwater heater outlet temperature to a fixed value. It is important to fix the feedwater heater outlet temperature since the outlet of the feedwater heater is mixed with the saturated liquid from the outlet of the steam separator. According to the solar resources, outlet flow rate of the saturated liquid from the steam separator changes since the outlet quality is changing. So that with a fixed feedwater heater outlet temperature, the inlet to the preheating and boiling sections of the solar collector arrays changes according to solar resources. When DNI is low, the mass flow rate of the condensed liquid increases which makes the inlet temperature to the preheater and boiling sections increase. The second assumption is simulating the outlet behavior of the system according to changing solar resources. In this second assumption, the feedwater heater outlet temperature is fixed to 115 °C which is defined as the solar field inlet temperature in [21]. The mass flow rate of the feedwater outlet is arranged to be the previously defined mass flow rate after being mixed with the condensed liquid from the steam separator.

The mass flow rate for the 7 parallel loops of collectors simulated is,

$$\dot{m} = 1.42 \times (7\text{loops}) = 9.94 \text{ kg/s} \quad (4.2)$$

For both cases Almeria Airport TMY2 weather data are used. Table 4.1 presents the geographical information. The results are compared with the reference simulation done for PSA site located at approximately N 37° 5' and 2° 21'. Specifically, the Almeria Airport is

approximately 165 km south of the reference simulation and is the closest location to the reference simulation for which the author had good meteorological (Meteornorm) data.

Figure 4.5 presents a sample TRNSYS model used in both cases for the simulations.

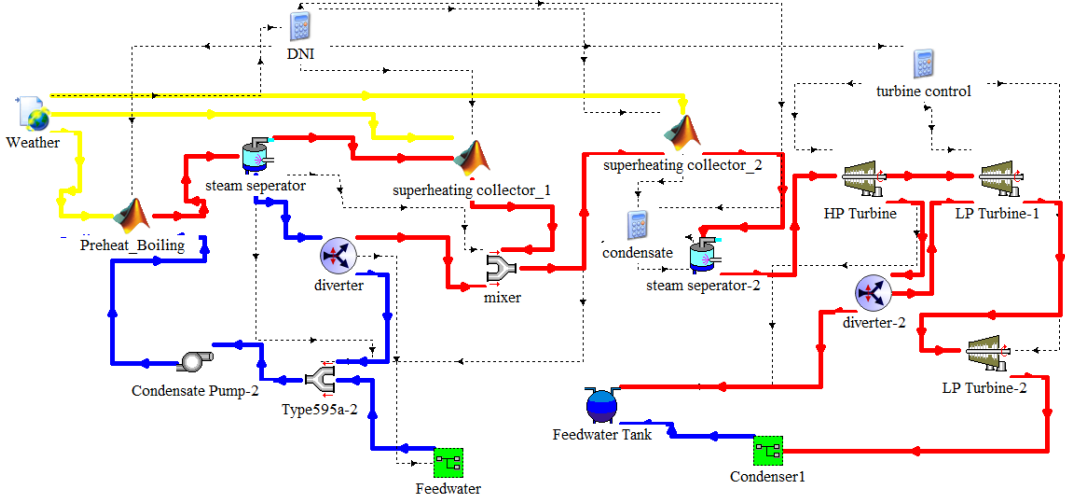


Figure 4.5 Sample TRNSYS Model Used in Both Cases of Simulation

As shown in Figure 4.5, there is an Equation type which includes an *if* statement for turbine control. This component stops the turbines when DNI = 0.

Component connections for the power plant model are shown in Table 4.4.

Table 4.4 Component Connections of Power Pant Model

#	Model Component	Trnsys Type	Input Connections			
			T	P	m	h
1	Preheat and Boiling	155	$T_{1,i} = T_{2,e}$	$P_{1,i} = P_{2,e}$	$m_{1,i} = m_{2,e}$	$h_{1,i} = h_{2,e}$
2	Feedwater Pump	15	$T_{2,i} = T_{9,e}$	$P_{2,i} = P_{9,e}$	$m_{2,i} = m_{9,e}$	$h_{2,i} = h_{9,e}$
3	Steam Separator-1	611	$T_{3,i} = T_{1,e}$	$P_{3,i} = P_{1,e}$	$m_{3,i} = m_{1,e}$	$h_{3,i} = h_{1,e}$
4	Diverter	11	$T_{4,i} = T_{3,el}$	$P_{4,i} = P_{3,el}$	$m_{4,i} = m_{3,el}$	$h_{4,i} = h_{3,el}$
5	Superheating Collector 1	155	$T_{5,i} = T_{3,ev}$	$P_{5,i} = P_{3,ev}$	$m_{5,i} = m_{3,ev}$	$h_{5,i} = h_{3,ev}$
6	Mixer	595	$T_{6,i1} = T_{4,e1}$ $T_{6,i2} = T_{5,e}$	$P_{6,i1} = P_{4,e1}$ $P_{6,i2} = P_{5,e}$	$m_{6,i1} = m_{5,e}$ $m_{6,i2} = m_{4,e1}$	$h_{6,i1} = h_{5,e}$ $h_{6,i2} = h_{4,e1}$
7	Superheating Collector 2	155	$T_{7,i} = T_{6,e}$	$P_{7,i} = P_{6,e}$	$m_{7,i} = m_{6,e}$	$h_{7,i} = h_{6,e}$
8	Feedwater					
9	Feedwater Heater	595	$T_{9,i1} = T_{4,e2}$; $T_{9,i2} = T_{8,e}$	$P_{9,i1} = P_{4,e2}$ $P_{9,i2} = P_{8,e}$	$m_{9,i1} = m_{4,e2}$; $m_{9,i2} = m_{8,e}$	$h_{9,i1} = h_{4,e2}$ $h_{9,i2} = h_{8,e}$
10	Steam Separator-2	611	$T_{10,i} = T_{7,e}$	$P_{10,i} = P_{7,e}$	$m_{10,i} = m_{7,e}$	$h_{10,i} = h_{7,e}$
11	HP Turbine	592c	$T_{11,i} = T_{10,e}$	$P_{11,i} = P_{10,e}$	$m_{11,i} = m_{10,e}$	$h_{11,i} = h_{10,e}$
12	Diverter-2	11	$T_{12,i} = T_{11,e}$	$P_{12,i} = P_{11,e}$	$m_{12,i} = m_{11,e}$	$h_{12,i} = h_{11,e}$
13	LP Turbine-1	592c	$T_{13,i} = T_{12,e1}$	$P_{13,i} = P_{11,e}$	$m_{13,i} = m_{12,e1}$	$h_{13,i} = h_{11,e}$
14	LP Turbine-2	592c	$T_{14,i} = T_{13,e}$	$P_{14,i} = P_{13,e}$	$m_{14,i} = m_{13,e}$	$h_{14,i} = h_{13,e}$
15	Condenser		$T_{15,i} = T_{14,e}$	$P_{15,i} = P_{14,e}$	$m_{15,i} = m_{14,e}$	$h_{15,i} = h_{14,e}$
16	Feedwater Tank	640	$T_{16,i1} = T_{12,e2}$ $T_{16,i2} = T_{15,e}$	$P_{16,i1} = P_{12,e2}$ $P_{16,i2} = P_{15,e}$	$m_{16,i1} = m_{12,e2}$ $m_{16,i2} = m_{15,e}$	$h_{16,i1} = h_{12,e2}$ $h_{16,i2} = h_{15,e}$

Subscripts: i= inlet, e=outlet, l=liquid, v=vapor, e1= first outlet

In this work, two different dates are simulated which are chosen to be nearly the same day with the reference simulation data. This is important for simulating similar solar angles as in the reference simulation. The second important factor for date selection is the DNI. Two dates are selected in the TMY2 data for Almeria Airport where the hourly DNI distribution is closest to the reference simulation data presented in the INDITEP project.

In the simulations done here, as stated above, weather data and dates are similar to but not identical to that in the published simulation data. For this reason, it is important to present the distributions of DNI for both the TMY2 data used in this work and the data used in the reference simulation.

Figure 4.6 presents DNI for TMY2 Data and Reference Simulation for June 12 and overall acceptable agreement is found.

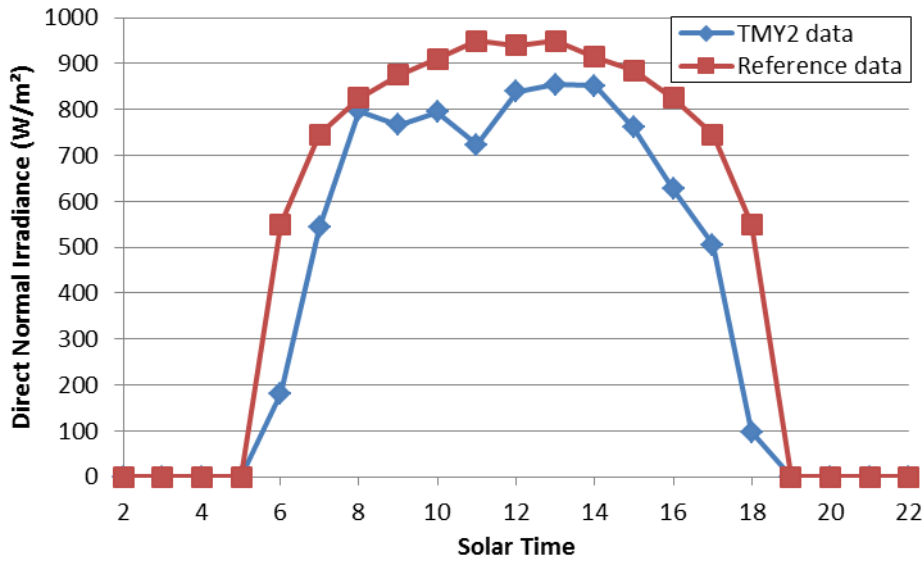


Figure 4.6 DNI for TMY2 Data and Reference Simulation for June 12

The Results for case 1, where the inlet temperature for preheating and boiling section are constant at 153°C, for June 12 are presented in Figure 4.7.

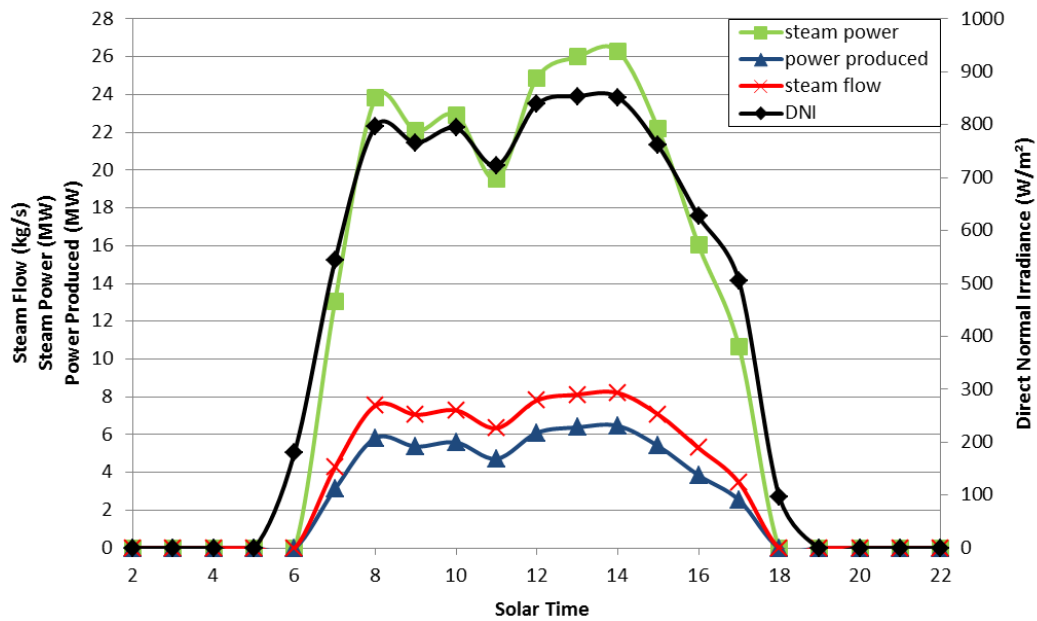


Figure 4.7 Simulation Result of June 12 for Almeria Airport TMY Data (case 1)

In order to compare the results with the published data, Figure 4.8 shows the simulation results for June 12 published for PSA site geographical data.

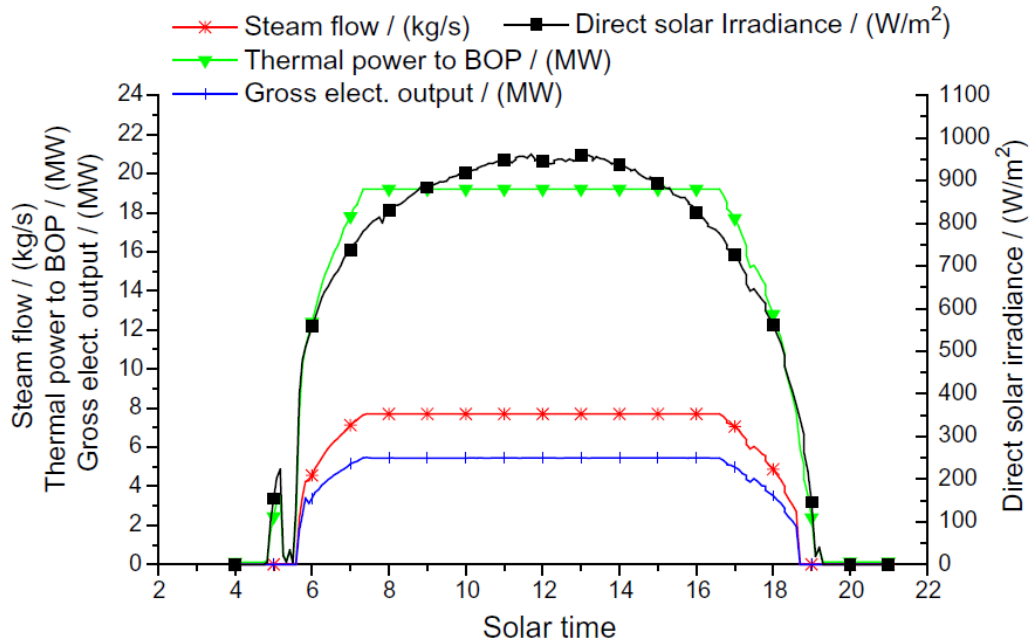


Figure 4.8 Published Simulation Results of June 12 for PSA Site [21]

In Figure 4.8, for the published data, the simulation fixed the maximum power output to 5 MWe and the excess thermal power is dumped, possibly by defocusing some of the collectors. If the simulation results are compared with the published data, between 6-8 MW turbine power is produced which is capable of producing 5 MW if a control system is adapted to the system to set a maximum power as in the published simulation.

Due to decrease in the DNI at 11 AM, the steam power also decreases. This decrease in the DNI is likely due to clouds at this time.

Figure 4.9 presents the simulation result for the second case on June 12. In this case, the feedwater outlet temperature was fixed to 115 °C.

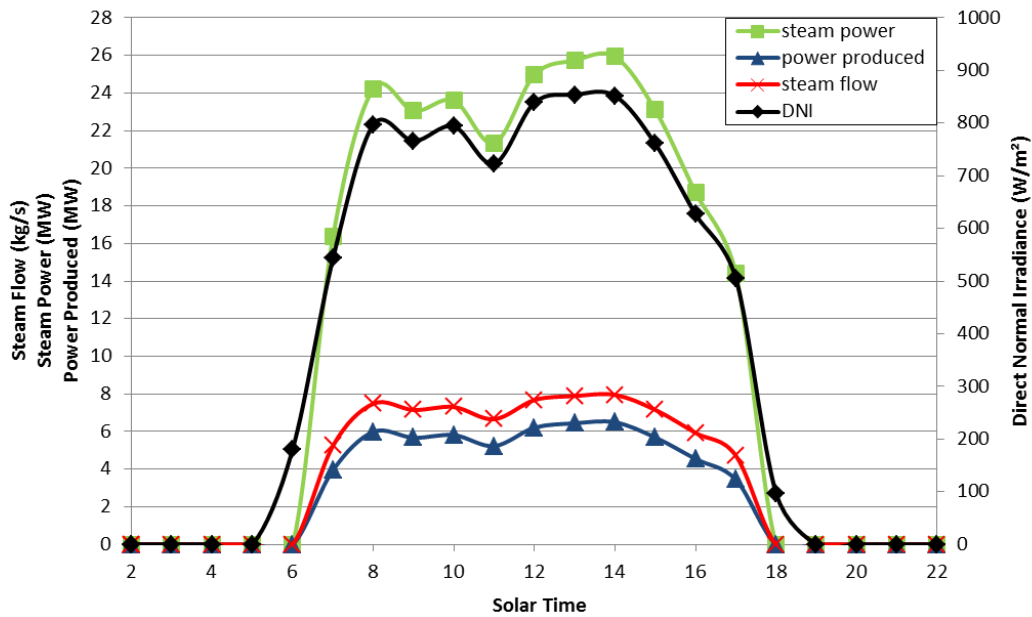


Figure 4.9 Simulation Result of June 12 for Almeria Airport TMY Data (case 2)

In case 2 the collect temperatures to the preheat and boiling section increase to 200-220 °C so that the outlet temperature and enthalpy become higher than that required since the feedwater heater has also an input from the condensed liquid at about 290°C. If we compare the results with case 1, the results are slightly higher. But it can be explained due to the high inlet temperature. In the second case, the power output from the power block is a little higher than 6 MW for the best hour which is 4 pm.

June 12 is selected since that date was the same as the reference data and is a good summer day in terms of solar resources. Figure 4.10 presents the DNI for both TMY2 data and reference data on June 12.

Another date also presented by the reference project was January 29. In order to compare both case 1 and case 2 with the published data, a good winter day close to the reference simulation date, February 3 is presented. This date is selected because this was a close date to the published data date and had identical solar resources. Figure 4.10 shows distribution of DNI for both the present simulated and published simulation data.

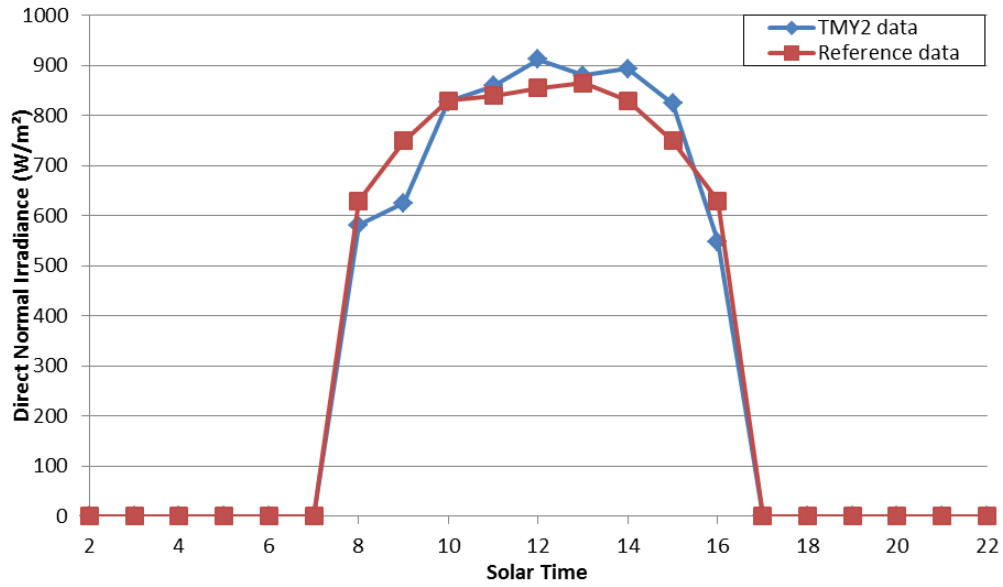


Figure 4.10 DNI for TMY2 Data and Reference Simulation for Clear Winter Day (February 3-January 29)

Figure 4.11 presents the case 1 results with a constant 153 °C inlet temperature to the preheater and boiling section for February 3.

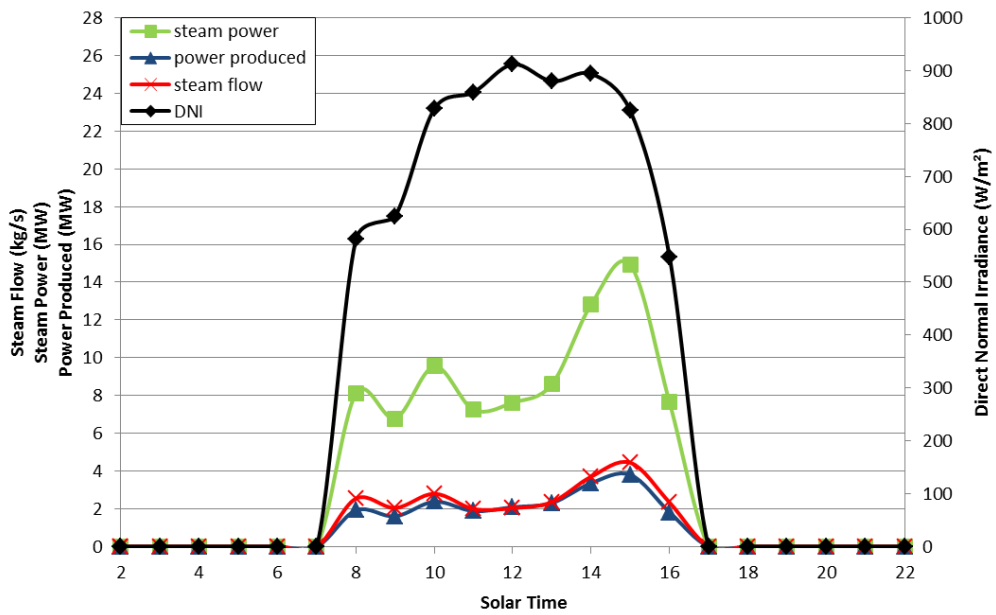


Figure 4.11 Simulation Result of February 3 for Almeria Airport TMY Data (case 1)

Figure 4.12 presents the results for January 29 published for PSA site geographical data.

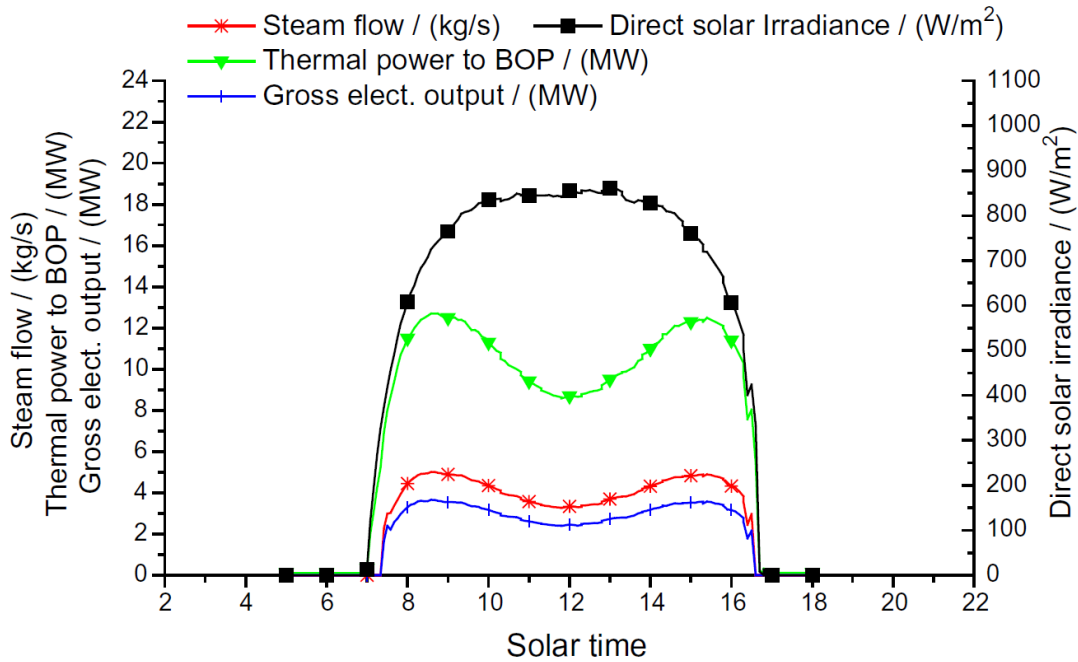


Figure 4.12 Published Simulation Results of January 29 for PSA Site [21]

In Figures 4.11 and 4.12, the DNI distribution is slightly different. But a comparison can be made at 10 AM and 1 PM when the DNI for both the present and reference simulations are identical.

In Figure 4.12, for 10 AM, approximately 11 MW of steam power is produced in the reference published simulation results. In the simulations done here, shown in Figure 4.11, the thermal power produced is 9.54 MW, which corresponds to a 13.2 % difference between the simulation results and the reference simulations. The published results are higher also in terms of steam flow produced. At 10 AM, approximately 4 kg/s steam is produced in the reference simulation data. In the simulation presented in this work, 2.8 kg/s of steam is produced. The main reason for the differences in the steam mass flow rate is the exit temperature. Although the exit temperatures are not presented in the reference simulation, in the design conditions it is assumed as 410 °C [21]. In the simulations presented here, the exit temperatures are ranges from 414 °C to 650 °C according to the solar resources. In this case, a control system should be adapted to the system to adjust the injection rate in order to reduce the outlet temperature. For instance, at 10 AM, the simulation results show that steam with 500 °C exit temperature is produced. For the simulation presented here, the injection flow rate is fixed as 10 % of the saturated liquid flow rate leaving the separator. This temperature can be reduced by changing the injection rate.

In Figure 4.12, for 1 PM, approximately 9.5 MW of steam power is produced in the reference published simulation results. For the present simulations presented in Figure 4.11, 8.6 MW steam power is produced. This difference corresponds to 9.5 % difference between the published simulation results and simulation results presented in this thesis.

Figure 4.13 shows the simulation result for the second case on February 3. In this case, the feedwater outlet temperature is fixed at 115 °C.

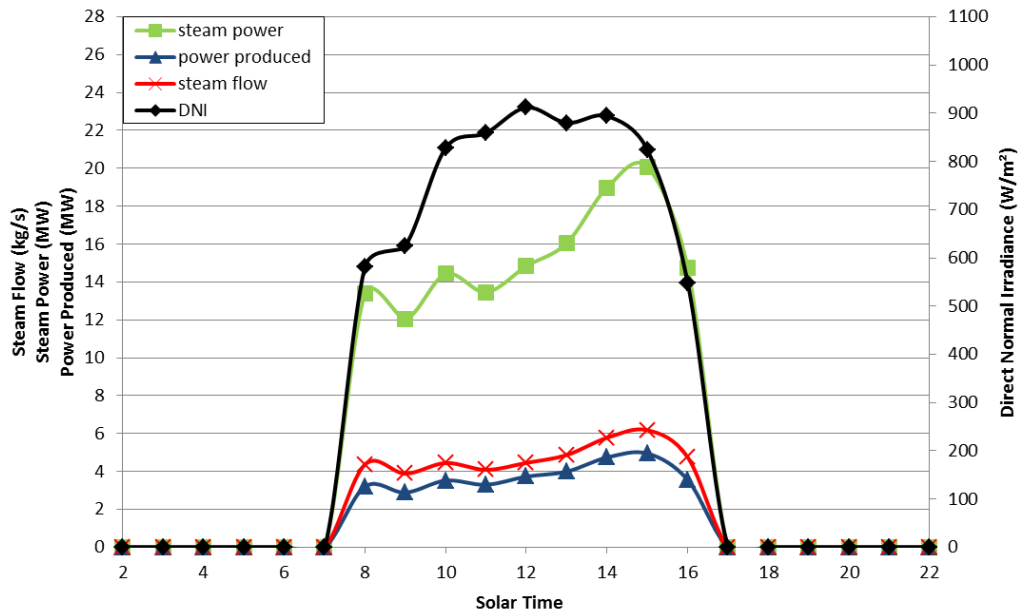


Figure 4.13 Simulation Result of February 3 for Almeria Airport TMY Data (case 2)

If Figures 4.13 and 4.11 are compared, due to the high inlet temperature to the preheating and boiling section of the solar field for the second case, the results are slightly higher. Additionally, at 10 AM, 14.42 MW steam power is produced while at 1 PM 16.05 MW steam power is produced.

In order to show the system performance, the system efficiency is calculated for June 12 solar noon for case-1, 153 °C inlet temperature to the preheating and boiling section of solar array as summarized in Table 5.1.

Table 4.5 Data Used for System Efficiency Calculations

DNI W/m ²	COS(θ)	Power Produced MW
839	0,9704	4,72

The system efficiency is calculated as,

$$\mu_{system} = \frac{Power\ Produced}{DNI\ cos\theta\ A} \tag{5.1}$$

In Equation 5.1, *A* is the sum of aperture areas. For 7 parallel loops of the solar field each having 10 collectors there is 548.35 m² aperture area for 1 collector, which makes the all collector field aperture area equal to 38384.5 m².

For solar noon for June 12, the total system efficiency is 15.1 %, which is a meaningful value since the field efficiencies are around 60-70 % and power block efficiency is around 25 %.

CHAPTER 5

CONCLUSION AND FUTURE WORK

Conventional Concentrating Solar Power (CSP) plants with parabolic trough collectors (PTC's) use synthetic oil as the heat transfer fluid (HTF). Unlike water, many HTF's have temperature limitations and harm the environment. In order to drive a steam turbine the thermal energy of the HTF must be transferred to water. In this case, the efficiency drops due to the usage of heat exchangers. Generating steam directly inside PTC's (Direct Steam Generation, DSG) can be an alternative to using HTF's. In this thesis, a mathematical model of a (PTC) with Direct Steam Generation (DSG) is presented.

The mathematical model of the DSG collector array presented in this thesis is based on the solar array presented in [21]. The two phase heat transfer model is adapted from [22]. For the two phase pressure drop model, the Friedel correlation is used. The mathematical model was run for design conditions stated in [21] and the results are compared. Good agreement is found between the published data and the simulation results.

In order to show how a DSG solar collector array reacts to different inlet conditions, parametric studies are done. The model is run for different inlet temperatures with two different cases. In the first case different working pressures are simulated. In the second case different solar resources are also simulated. The results of DSG simulations show that for lower working pressures, the overall efficiency is higher due to lower saturation temperature of the water, and consequently lower temperatures and thermal losses in the 2-phase part of the collector.. On the other hand, for lower working pressures the pressure drops are higher which can cause increase the required pumping power. As a result for such a system there is a tradeoff between overall efficiency and internal energy consumption. For low solar resources, if the inlet temperature is below a certain value, very low quality steam can be produced. After the steam/liquid separation process, pure steam with a low mass flow rate is passed through the superheating collectors, and the steam can be heated up much higher than required and can be harmful for far components.

The DSG mathematical model programmed in Matlab is then linked to TRNSYS 17 software [35]. Since steam is needed in industry in addition to being used to produce electricity, a solar array used to produce steam is simulated. Results are presented and discussed.

A CSP plant using DSG technology is simulated using TRNSYS 17. To have the model be stable, one of two assumptions is used. For the first case, the inlet temperature to the collectors is kept constant and equal to the design conditions. In the second case, the

feedwater temperature is kept constant which results in inlet temperature to the collector field that varies with the solar resources. Results are compared with the published data in [21]. Better agreement is found for the first case. In the second case, the inlet temperatures become too high which causes the predicted outputs to also be too high.

The present work builds on and extends Usta's work [27], who was the first person at Middle East Technical University to model and simulate a CSP system using TRNSYS. As with any research, there are many opportunities to further extend the present research.

The present model does not have a control system which sets the inlet temperature to the collectors according to the solar resources or adjusts the active collectors at any instant. A control system for the present model can be adapted to the existing model so that constant outputs rather than fluctuating power outputs can be reached. Using a control strategy, such as setting the outlet temperature to the design point outlet temperature of 410 °C, will decrease the differences in the mass flow rates between the published simulation results and simulation results presented here.

The present model does not include thermal energy storage (TES). With TES, the power plant simulated in this work can store solar energy during the day and use this stored solar energy to produce electricity after the sun sets and therefore improve the system's capacity factor and dispatchability. Significant work remains for optimum the design, sizing and control of CSP plants with TES.

Hybridization of conventional power plants (e.g., combustion or geothermal) with CSP can also result in high capacity factors and dispatchability while reducing the power plant's environmental impact. Studies into modeling and simulating the hybrid systems are required to identify the best designs, quantify their performance, and understand how these system's may operate.

Modeling and simulating a CSP plant using a HTF and comparing the results to DSG technology can give more insight into the advantages and disadvantages of each technology.

REFERENCES

- [1] Y. Heper, "Steam power plant engineering course lecture notes, Middle East Technical university," 03-2011.
- [2] "co2highlights.pdf." [Online]. Available: <http://www.iea.org/co2highlights/co2highlights.pdf> [Accessed: 03-Mar-2013].
- [3] A. Fernández-García, E. Zarza, L. Valenzuela, and M. Pérez, "Parabolic-trough solar collectors and their applications," *Renewable and Sustainable Energy Reviews*, vol. 14, no. 7, pp. 1695–1721, Sep. 2010.
- [4] "Nothing new under the sun?: solar heating's Philadelphia story | NFR." [Online]. Available: <http://ruins.wordpress.com/2010/05/04/nothing-new-under-the-sun-solar-heatings-philadelphia-story/>. [Accessed: 03-Mar-2013].
- [5] S. R. Wenham, M. A. Green, M. E. Watt, R. Corkish, and A. Sproul, Eds., *Applied Photovoltaics*, 3rd ed. Routledge, 2012.
- [6] A. Esper and W. Mühlbauer, "Solar drying - an effective means of food preservation," *Renewable Energy*, vol. 15, no. 1–4, pp. 95–100, Sep. 1998.
- [7] S. Kalogirou, *Solar Energy Engineering: Processes and Systems*. Academic Press, 2009.
- [8] "World's Largest Commercial Solar Power Tower Goes Online - CleanTechnica." [Online]. Available: <http://cleantechnica.com/2009/04/29/tower-of-power/>. [Accessed: 03-Mar-2013].
- [9] K. Lovegrove, G. Burgess, and J. Pye, "A new 500 m² paraboloidal dish solar concentrator," *Solar Energy*, vol. 85, no. 4, pp. 620–626, Apr. 2011.
- [10] X. Wei, Z. Lu, Z. Wang, W. Yu, H. Zhang, and Z. Yao, "A new method for the design of the heliostat field layout for solar tower power plant," *Renewable Energy*, vol. 35, no. 9, pp. 1970–1975, Sep. 2010.
- [11] Craig E., Sutherland J. Paul, Gould, and Jr. William R., "Solar Two: A Molten Salt Power Tower Demonstration*."
- [12] "2006_ps10.pdf." [Online]. Available: http://ec.europa.eu/energy/renewables/solar_electricity/doc/2006_ps10.pdf. [Accessed: 03-Mar-2013].

- [13] "Concentrating Solar Power." [Online]. Available: <http://www.greenchipstocks.com/articles/concentrating-solar-power/86>. [Accessed: 03-Mar-2013].
- [14] D. Mills, "Advances in solar thermal electricity technology," *Solar Energy*, vol. 76, no. 1–3, pp. 19–31, Jan. 2004.
- [15] "DLR Portal - Inauguration of new Fresnel collector at Plataforma Solar de Almería in Spain." [Online]. Available: http://www.dlr.de/en/DesktopDefault.aspx/tabid-4530/3681_read-9671/gallery-1/gallery_read-Image.1.3622/. [Accessed: 03-Mar-2013].
- [16] "Amargosa Valley Solar Millennium Scoping Meeting August 2009." [Online]. Available: <http://www.basinandrangewatch.org/AV-SolarMill-scoping-Aug2009.html>. [Accessed: 03-Mar-2013].
- [17] "NREL: TroughNet - U.S. Parabolic Trough Power Plant Data." [Online]. Available: http://www.nrel.gov/csp/troughnet/power_plant_data.html. [Accessed: 13-Jan-2013].
- [18] A. Press, "Storage Tank at Solar Power Plant in Desert Explodes; Immediate Area Is Evacuated," *Los Angeles Times*, 27-Feb-1999.
- [19] M. Eck and W.-D. Steinmann, "Direct Steam Generation in Parabolic Troughs: First Results of the DISS Project," *Journal of Solar Energy Engineering*, vol. 124, no. 2, p. 134, 2002.
- [20] L. Valenzuela, E. Zarza, M. Berenguel, and E. F. Camacho, "Control scheme for direct steam generation in parabolic troughs under recirculation operation mode," *Solar Energy*, vol. 80, no. 1, pp. 1–17, Jan. 2006.
- [21] E. Zarza, M. E. Rojas, González, L. Ibez, J. Caballero, M^a, and F. Rueda, "INDITEP: The first pre-commercial DSG solar power plant," *Solar Energy*, vol. 80, no. 10, pp. 1270–1276, 2006.
- [22] S. D. Odeh, G. L. Morrison, and M. Behnia, "Modelling of parabolic trough direct steam generation solar collectors," *Solar Energy*, vol. 62, no. 6, pp. 395–406, Jun. 1998.
- [23] Clifford K. Ho, "Software and Codes for Analysis of Concentrating Solar Power Technologies." Sandia National Laboratories.
- [24] Lippke, F., "Simulation of the Part Load Behavior of a 30 MWe SEGS Plant." Sandia National Laboratories, 1995.
- [25] Jones Scott A., Pitz-Paal Robert, Schwarzböezl Peter, Blair Nathan, and Cable Robert, "Trnsys Modeling of the SEGS VI Parabolic Trough Solar Electric Generation System," *Proceedings of Solar Forum 2001*, Apr. 2001.
- [26] Patnode Angela M., "Simulation and Performance Evaluation of Parabolic Trough Solar Power Plants," Master Thesis, University of Wisconsin-Madison, 2006.

- [27] Usta Yasemin, "Simulations of a Large Scale Solar Thermal Power Plant in Turkey Using Concentrating Parabolic Trough Collectors," Master Thesis, Middle East Technical University, 2010.
- [28] J. A. Duffie and W. A. Beckman, *Solar Engineering of Thermal Processes*, 3rd ed. Wiley, 2006.
- [29] "Insolation." [Online]. Available: <http://www.geog.ucsb.edu/ideas/Insolation.html>. [Accessed: 06-Feb-2013].
- [30] T. L. Bergman, A. S. Lavine, F. P. Incropera, and D. P. DeWitt, *Fundamentals of Heat and Mass Transfer*, 6th ed. Wiley, 2007.
- [31] R. W. Fox and A. T. McDonald, *Introduction to fluid mechanics*. Wiley, 1985.
- [32] Thome, John R., "Wolverine Tube, Inc. Engineering Data Book III." .
- [33] Moreno Quiben Jesus, "Experimental and Analytical Study of Two-Phase Pressure Drops During Evaporation in Horizontal Tubes," PhD Thesis, École Polytechnique Fédérale de Lausanne, 2005.
- [34] "X Steam, Thermodynamic properties of water and steam. - File Exchange - MATLAB Central." [Online]. Available: <http://www.mathworks.com/matlabcentral/fileexchange/9817>. [Accessed: 13-Mar-2013].
- [35] Klein, S.A. et al, TRNSYS 17: A Transient System Simulation Program. Solar Energy Laboratory, University of Wisconsin, Madison, USA, <http://sel.me.wisc.edu/trnsys/>, 2010.